Fall 2009

Focusing Electromagnetic Radiation in Dielectric Media

Mark A. Migliaccio Jr.
Old Dominion University

Recommended Citation

Migliaccio, Mark A.. "Focusing Electromagnetic Radiation in Dielectric Media" (2009). Master of Science (MS), Thesis, Electrical & Computer Engineering, Old Dominion University, DOI: 10.25777/8f15-c005
https://digitalcommons.odu.edu/ece_etds/443

FOCUSING ELECTROMAGNETIC RADIATION IN DIELECTRIC MEDIA

by

Mark A. Migliaccio Jr.
B.S. 2008, Old Dominion University

A Thesis Submitted to the Faculty of
Old Dominion University in Partial Fulfillment of the
Requirement for the Degree of

MASTER OF SCIENCE

ELECTRICAL ENGINEERING

OLD DOMINION UNIVERSITY
December 2009

Approved by:

Shu Xiao (Director)

Karl Schoenbach (Member)

Juergen Kolb (Member)

ABSTRACT

FOCUSING ELECTROMAGNETIC RADIATION IN DIELECTRIC MEDIA

Mark A. Migliaccio Jr.
Old Dominion University, 2009
Director: Dr. Shu Xiao

Bioelectrics and microwave imaging requires an ultra-wideband (UWB) antenna to deliver intense, short electromagnetic pulses into biological targets for the purpose of therapy and imaging. Two antennas with different focal distances, predicted by a two-dimensional model, have been designed for focusing electromagnetic radiation in the near field.

Focusing is achieved through the use of prolate spheroidal reflector antennas with a conical wave launcher submerged in water. For an ultra-wideband feed signal, with a rise time of 200 picoseconds, the maximum electric field was found to be close to the edge of the reflector, a result that differs from the modeled results. When narrowband signals of 900 MHz and 1500 MHz are fed to the antenna, electric fields have been shown to focus near the focal point.

I would like to dedicate this thesis to all my family and friends who have supported me and have constantly lifted me up with their kind words of encouragement. I especially dedicate this to Julia for her encouragement, support and love.

ACKNOWLEDGMENTS

I would like to acknowledge Dr. Shu Xiao for his support and guidance during this research project. I would like to thank Dr. Carl Baum for his expertise and guidance on the development of the antenna, and Dr. Karl Schoenbach and Dr. Juergen Kolb for agreeing to be on the thesis committee.

I would like to thank Dr. Lars Ludeking and Andy Woods for providing guidance and feedback to help with learning the MAGIC modeling software.

I would like to thank my fellow graduate students Thomas Camp and Chandra Bajracharya for their valuable input and assistance.

TABLE OF CONTENTS

Page

Section

Page

Page

LIST OF TABLES

LIST OF FIGURES

Figure Page

Page

Page

Page

SECTION 1

INTRODUCTION

Over the past few years, interest has increased in the field of bioelectrics—the study of the effects of ionized gases and short pulses of intense energy on biological systems, and the application of that research. The current method to apply these ultra-short pulses is through needle electrodes and metal parallel plate electrodes [1]. There has been recent interest in applying these pulses non-invasively through the use of an antenna that could focus such intense pulses to a deeper target volume for therapy and imaging [2-3].

1.1. Therapeutic Effects of Ultra-Short Pulses

When sub-microsecond pulses are applied to the biological samples, the cells can be described in terms of resistances and capacitances. The bi-lipid plasma membrane surrounding the cell acts as a capacitor, and the interior of the cell—cytoplasm and organelles—acts as a resistive component. Under resistor-capacitor circuit theory, this gives the cell a certain time constant. The time constant describes the amount of time necessary to charge the plasma membrane. When the pulse duration is decreased to a pulse width that is less than the time constant of the plasma membrane, then the plasma membrane is largely unaffected by the pulse and the effects of these faster pulses can be applied directly to the organelles in the cell.

There have been significant findings involving the application of sub-microsecond pulses to induce a number of effects on biological systems. The application

---

This paper formatted using IEEE Editorial Style Manual.

of these extremely short pulses at very high voltages was used to treat melanoma tumors on mice. One treatment reduced the tumor size significantly, and a second treatment delayed by a week resulted in the complete removal of the tumor [4]. Treatment with 300 nanosecond pulses with an electric field strength of 40 kV/cm were effective in the removal of the tumor. The results of mice that received treatment for a tumor were still in remission at least six months after the last treatment. Studies have shown that by applying these intense pulses to biological systems, the cells show an increase in the release of calcium. It is thought that this calcium release signals the cell to perform certain tasks, such as to begin programmed cell death, or apoptosis, and attributes to the aggregation of platelets [5-7].

While most of the research has focused on the effects of sub-microsecond pulses, recently sub-nanosecond pulses have been researched to study their effects on programmed cell death and platelet activation, among other biological effects [3]. Sub-nanosecond pulses allow for the study of the dielectric phenomena of cells, in which the distribution of the electric field is determined mostly by the dielectric permittivity of the cell structure. Here, the electric field permeates the cell much more than for sub-microsecond pulses [2-3, 8]. Therefore, the sub-nanosecond pulse regime may cause a more direct effect on the intracellular organelles.

A sub-nanosecond high-voltage pulse generator capable of delivering ultra-short pulses with pulse durations as short as 150 picoseconds, and pulse rise times of about 100 picoseconds, has been developed. This pulse generator is capable of producing intense pulses with voltages as high as 120 kilovolts [9]. Such short pulses could possibly be used for therapeutic applications through an ultra-wideband, high-power antenna, which radiates and focuses those pulses onto a target volume.

1.2. Imaging with Ultra-Wideband Electrical Pulses

Besides therapeutic applications, ultra wideband (UWB) pulses can be used to probe tissue dielectric properties. The electrical properties of tissues, including conductivity and permittivity, differ depending on the type of tissue [10]. There is also a difference between the dielectric properties of normal, benign, and malignant tissue when measured at high frequencies, as shown in fig. 1 [11]. For the breast, the tissue is made up of adipose, glandular, and fibroconnective tissue. A three-dimensional dielectric characterization of a target, such as a tumor, is possible through the use of UWB radar elements by observing the backscattered signals from the target [12]. The use of a microwave imaging system, similar to ground penetrating radar, can detect varying dielectric properties of a spherical tumor 2 millimeters in diameter with a depth up to 5 centimeters below the skin [13-17]. The use of an ultra-wideband, high-power focusing antenna may allow for the detection of these dielectric properties of targets located deeper into the body.

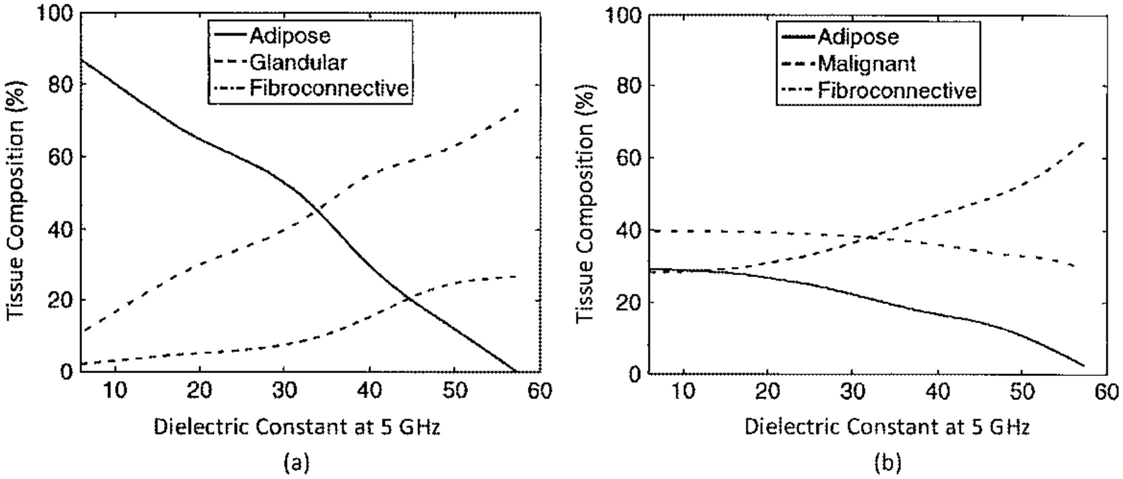

Figure 1: Composition of (a) normal and (b) cancerous tissue as a function of dielectric constant [11].

1.3. Thesis Objective

In bioelectrics, short electric pulses are delivered to the lesion site through contact electrodes such as a needle or plate-type electrode. To eliminate the use of electrodes and to possibly deliver these short electrical pulses to targets situated deeper in the body, an antenna should be developed. This antenna could focus the pulsed radiation and achieve the therapeutic purpose. Simultaneously, the antenna could be used to monitor the treatment efficacy and image the tissue dielectric properties. The goal of this thesis is to design and investigate a UWB antenna that focuses high-power, sub-nanosecond pulses. This design should eliminate the need to apply needle and plate-type contact electrodes that are uncomfortable and intimidating to patients receiving such high-voltage therapeutic treatments. It should also allow for the possibility of imaging using sub-nanosecond pulses by achieving high resolution focusing at a target. Such focusing, in conjunction with signal processing techniques, could result in a functional dielectric image of targeted tissue.

SECTION 2

BACKGROUND

2.1. UWB Pulses

An ultra-wideband signal is defined by the Federal Communications Commission (FCC) as radiation from an antenna with bandwidth that exceeds 500 MHz or a fractional bandwidth of greater than or equal to 20 percent [18]. Fractional bandwidth can be defined as in equation 2.1.1 for a sinusoidal signal or 2.1.2 for a carrier-free non-sinusoidal signal. Here Δf is the difference between the upper, f_H, and lower, f_L, frequencies of the signal, or the absolute bandwidth, and f_c is the center frequency. According to the definition above, the signal is classified as a UWB signal if the fractional bandwidth, η, is greater than 0.2 [19].

$$\eta = \frac{\Delta f}{f_c}, 0 < \eta < 1 \tag{2.1.1}$$

$$\eta = \frac{f_H - f_L}{f_H + f_L}, 0 < \eta < 1 \tag{2.1.2}$$

In the simplest form the electric and magnetic fields of an ultra-wideband pulse can be described by the radiation principle, in which the electric and magnetic field strength of a current over a Hertzian dipole is proportional to the first time derivative of the current, as shown in equation 2.1.3 [19].

$$(E, H)_{far\ field}\, \alpha \frac{di(t)}{dt} \tag{2.1.3}$$

To radiate an ultra-wideband pulse, the input signal that is differentiated from the antenna must have a rise time in the nanosecond and picosecond ranges [20]. An ideal step function signal when radiated from an antenna would create a pulsed electric field, as shown in fig. 2.

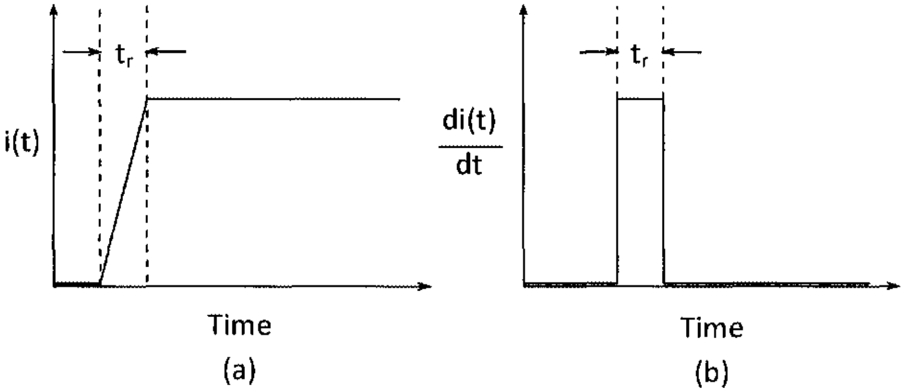

Figure 2: (a) Ideal step function current over Hertzian dipole and (b) ideal radiated UWB electric field pulse.

The ultra-wideband pulse can be approximated by a Gaussian waveform, as shown in equation 2.1.4, where A is the intensity of the electric field, and ΔT is the pulse duration.

$$\Omega(t) = Aexp[-4\pi(t/\Delta T)^2] \tag{2.1.4}$$

A UWB pulse has short pulse duration in the time domain. When transformed into the frequency domain, it is evident that an ultra-wideband pulse encompasses a wide range of frequencies. An example of an ultra-wideband pulse in the time domain and frequency domain is shown in fig. 3.

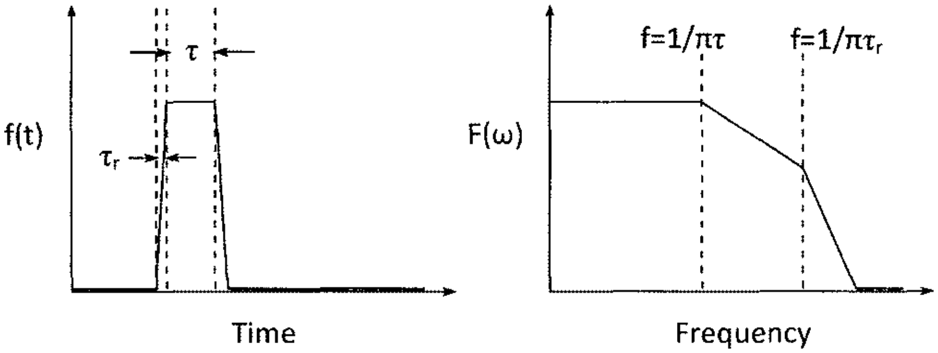

(a) (b)

Figure 3: Ultra-wideband pulse in the (a) time domain and (b) frequency domain.

2.2. UWB Antenna Origins

UWB antennas have been discussed as a means of electromagnetic propagation since at least 1898, when they were first investigated for the use of high-frequency transmission of radio waves for television [21]. Oliver Lodge, while authoring a patent for narrowband radio transmission, set the stage for UWB. He described capacitor areas where metal dipoles in some form; spherical, square plates; or other shapes may be used as transmitters and receivers. Lodge preferred triangular plates and biconical elements due to the low resistance and high capacity of the design. Some of his drawings from the patent, shown in fig. 4, are remarkably similar to bow-tie antenna elements that are in use today [22].

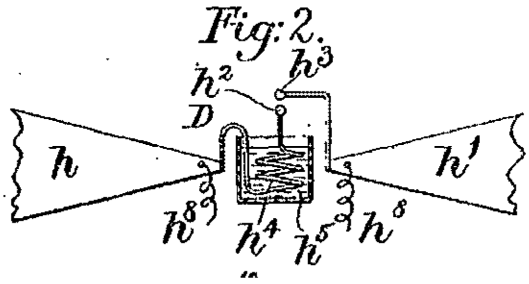

Figure 4: Lodge's capacitor area antenna element with spark gap.

In 1939 Carter revisited Lodge's designs for the biconical antenna elements. One of the important contributions of his patent was to incorporate a transmission line feed structure instead of the common spark gap. Two of his designs included a transmission line fed through one cone to the central feed point, shown in fig. 5 [23]. Another design included a conical monopole, an element that involved a transmission line-fed cone radiating over a ground plane. Carter improved upon Lodge's biconical antenna elements to include a tapered feed that replaced the spark gap.

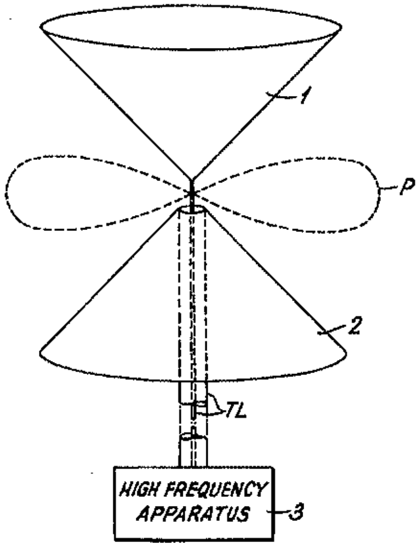

Figure 5: Carter's biconical antenna element with transmission line feed, hollow cones (1 and 2), remotely located transmitter (3), and radiation pattern (P).

2.3. UWB Antennas

One type of antenna useful for ultra-wideband applications is the patch antenna. This antenna element can be constructed using printed circuit board techniques, where a dielectric substrate layer is on top of a ground plane. On top of the substrate a radiator, at least half a wavelength long, can be etched into a certain shape. The radiation is generated around the edge of the conducting sheet. The radiation from such an element is orthogonal to the conducting surface of the antenna [24]. A simple patch antenna may not radiate the entire bandwidth necessary for a UWB signal. These elements can be modified using techniques such as creating stacks of carefully designed complex patch antennas to allow for UWB radiation [25].

Self-scaling geometries can result in an antenna that is theoretically independent of frequencies. According to Rumsey's principle, if an infinitely long antenna can be described by angles only, then it becomes independent of frequency [26]. This is due to the self-scaling properties of such radiators. Practically, it is impossible to create an infinitely long antenna, but for an antenna whose length appears to be long compared to the wavelength, the radiation is mostly independent of frequency [27]. It then can act as a high-pass filter, where the length of the radiator determines the lower frequency of the bandwidth of the antenna element. One example of a practical application is the bowtie antenna, shown in fig. 6, in which one triangular piece acts as the effective ground and the other triangular piece carries the signal. Antennas with a self-complementary structure are also frequency-independent and have constant input impedance. Such antenna elements can have a log-periodic truncated structure [28].

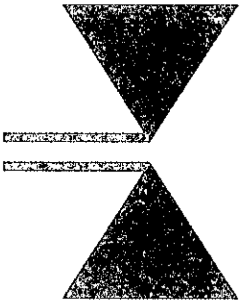

Figure 6: Bowtie antenna.

Another type of UWB antenna is the aperture class—which includes the slot antenna, waveguides, reflectors, and horn elements. One of the more heavily investigated types is the slot-type antenna element [29-34]. Generally, a slot antenna consists of a metal sheet that has a slot cut out, which could be of a variety of shapes and sizes. The radiation pattern for some antenna structures can be described by superimposing the radiation pattern of dipoles based on the driving current. Other structures, such as these aperture antennas are complicated and the radiation pattern is more easily described by applying Huygen's principle on the structure by estimating the electric field at a well-defined surface [27]. These slot antennas have a planar profile and come in a variety of shapes depending on the application. One type of slot antenna is the impulse slot antenna, a hybrid of a biconical type of aperture antenna and a traditional tapered slot antenna. When the cones are essentially flattened and the slot is tapered, the resulting slot antenna can radiate with a similar radiation pattern. The benefit of such a slot antenna is that it can be placed on objects such as the wing of a fighter jet, as in fig. 7 [35]. However the length of the conductor must be at least as long as the lowest transmitting wavelength. This could be a problem in some applications, such as for therapy and imaging, where size is a constraining factor.

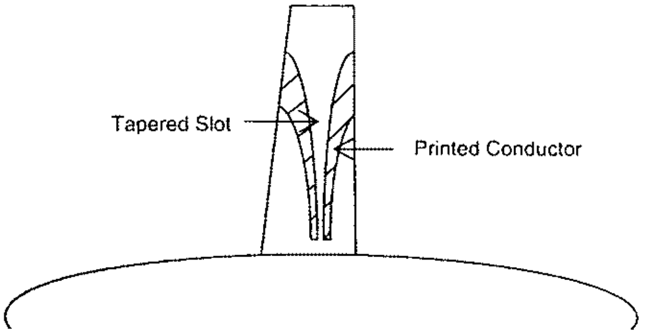

Figure 7: Possible setup for impulse slot antenna [35].

Another popular aperture antenna element used to deliver UWB signals is the transverse electromagnetic (TEM) horn element. The TEM horn antenna provides the benefit of broadband and non-dispersive qualities [36]. The antenna in general accepts a transmission line-fed signal and then radiates it outward in a tapered waveguide [37]. The tapering allows the "throat" of the horn to select the dominant mode. By choosing the correct flare angle, only the dominant mode will be able to freely propagate toward the aperture [38]. To minimize reflections the length of the tapered horn waveguide must be at least half a wavelength long. Again this causes the antenna element to be impractically long for some applications [36]. The wave front of these horn elements radiates a spherical TEM wave. In some cases, higher gain is required and a planar wave is more desirable [39].

To create a high-gain, planar wave front, Dr. Carl Baum invented another type of aperture antenna, called a reflector impulse radiating antenna (IRA) [40]. Various IRA designs have been used for applications such as ground penetrating radar to search for landmines and other buried objects, and non-lethal weapons [41-42]. A parabolic reflector with a TEM wave fed to the focal point of the parabola produces a planar wave front once the spherical wave reflects off the reflector surface. Such an antenna with feed arms that bring a fast step-function signal to the focus of the parabolic reflector is called a reflector IRA, shown in fig. 8 [39]. The feed arms are a self-reciprocating structure that simplifies the calculation of the electromagnetic fields [43]. The resulting far-field strength is proportional to the frequency [44]. Like the TEM horn antenna, the reflector IRA is non-dispersive, ultra-wideband, and directive, but instead produces a planar wave front [45]. Such an antenna can deliver high-power electric fields.

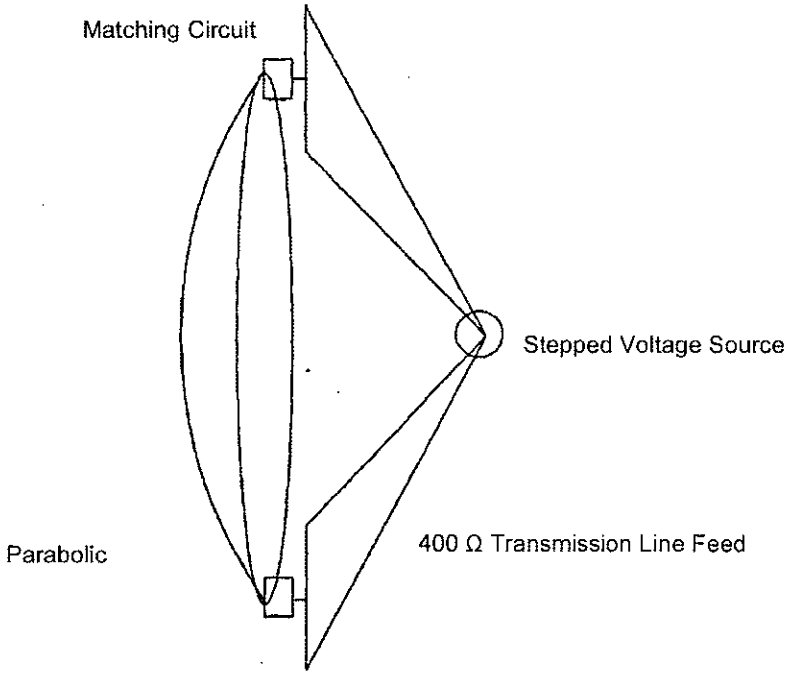

Figure 8: Carl Baum's reflector IRA [45].

2.4. Prolate Spheroidal Reflector IRA

In some instances it may be advantageous not only to be able to control the directivity of these impulses but to also focus them in the near-field. The definition of far-field distance can be described by equation 2.4.1, where R is the distance from a source to a receiving antenna, D is the diameter of the aperture of the antenna, and λ_0 is the free-space wavelength of the radiating field. The condition for near-field operation can be shown in equation 2.4.2. This criterion is determined by selecting a phase error of 22.5 degrees, or 1/16 of the free-space wavelength. For signals operating at distances lower than that value, the region is called the near-field [46].

$$R_{far-field} = \frac{2D^2}{\lambda_0} \tag{2.4.1}$$

$$R < \frac{2D^2}{\lambda_0} \tag{2.4.2}$$

A prolate spheroidal reflector IRA was designed to do focus radiation in the near-field [47]. Similar to the standard reflector IRA, TEM waves, generated by a voltage step function, are fed into the antenna at the focal point of the reflector to radiate an impulse [48]. Rather than introducing this signal at the focal point of a parabolic reflector, a prolate spheroidal reflector focuses the signal in the near-field [47]. The reflected voltage on the transmission line increases as the distance between the two focal points decreases [49]. A prolate spheroid describes the three-dimensional realization of an ellipse that has been revolved about the major axis of the ellipse. A balanced, four-arm feed structure is used to feed the signal to the first focal point. Experimentally, this antenna has shown to focus at the focal point, but with lower amplitude for the impulse than expected through analytical calculations [50]. The geometry of a prolate spheroidal reflector IRA is shown in fig. 9, where –f and +f are the two focal points.

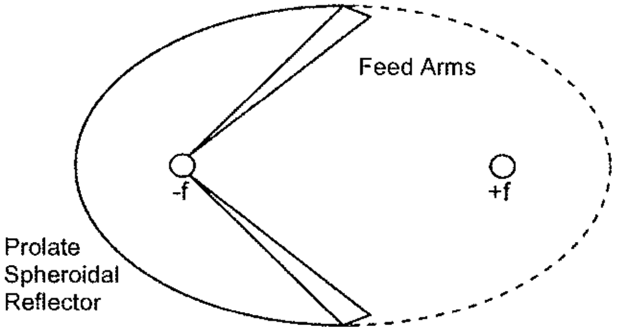

Figure 9: Prolate spheroidal reflector IRA geometry in 2-D.

2.5. Use of Dielectric Media to Enhance Antenna

One problem with trying to pass electromagnetic waves into the body is that the air-to-surface reflection at the skin often causes a large reflection of the wave energy, resulting in wasted energy [51]. Another issue is multipath propagation: Some waves may reflect off surfaces between the body and the antenna, and in most cases the waves travel around the body instead of through it [52]. These effects can be reduced, but not eliminated, by submerging the antenna and target tissue in water. The large reflection at the air-to-skin interface can be reduced in a water-to-skin interface, due to better energy coupling [51].

It is possible to compress the time-domain width of the impulse down to a size where a high resolution is obtained. The spatial width of a pulse, given by equation 2.5.1, is based on the velocity of the pulse, v, and the pulse duration, τ. The velocity of the pulse, v, can be described by the speed of light, C, the relative permittivity, ε_r, and relative permeability, μ_r, of the medium through which the pulse travels, as in equation 2.5.2.

$$p.w. = v\tau \tag{2.5.1}$$

$$v = \frac{c}{\sqrt{\mu_r \varepsilon_r}} \tag{2.5.2}$$

Increasing the dielectric properties of the medium through which the pulse is traveling can significantly decrease the spatial width of the impulse. If the pulse is radiated by the antenna in medium the spatial width of the wave is decreased by a factor of $\sqrt{\mu_r \varepsilon_r}$. To enhance this effect and decrease the focusing spot size of the radiated wave, a medium with a high dielectric permittivity is desirable. Water is one type of media with a high dielectric permittivity. With a relative permittivity of 81, the impulse spatial width of a signal radiated from a prolate spheroidal reflector IRA operating in water could be decreased by a factor of 9. This allows for the size of the antenna to be decreased by a factor of 9 as well [51].

2.6. UWB Antenna Summary

This survey of antennas shows that there are numerous methods available to deliver UWB pulses into tissue. The goal of this thesis is to design an antenna capable of focusing radiation on a target. The antenna designs discussed above can contribute to this antenna design. The most promising design would include an aperture antenna designed to focus high-intensity electric fields at a target.

To build a high-power system, the reflector IRA offers the best choice. To focus in the near field, a prolate spheroidal reflector should be used. However, the previously discussed prolate spheroidal reflector configuration uses a complex, four-arm balanced-feed structure. A spherical TEM wave can be more simply introduced at the first focal point by using a radiator that utilizes a transmission line feed. Specifically the conical monopole over a ground plane radiator offers this, while also having the benefit of being self-scaling and therefore frequency-independent. However, because of the finite dimensions of the cone, as discussed previously, the cone is not a good radiator for the lower frequencies included in a UWB pulse. Such a design would allow a high-voltage pulsed signal to be transmitted directly and simply from a coaxial transmission line to the conical radiator. This can decrease the complexity of the design.

Another challenge is to increase the resolution and decrease the size of the antenna. This can be done through manipulation of the UWB pulses using a medium with a high dielectric permittivity. In the case of water as the chosen medium, the antenna can be shrunk by a factor of 9, while reducing the wavelength of the pulse to less than 1 centimeter. One study has presented a novel design for a near-field focusing prolate spheroidal IRA that operates in water [53]. This antenna could operate in a medium with high dielectric permittivity to reduce the size of the antenna and the spatial width of the radiated pulses [54-55]. The geometry for such a prolate spheroidal reflector IRA is presented in fig. 10.

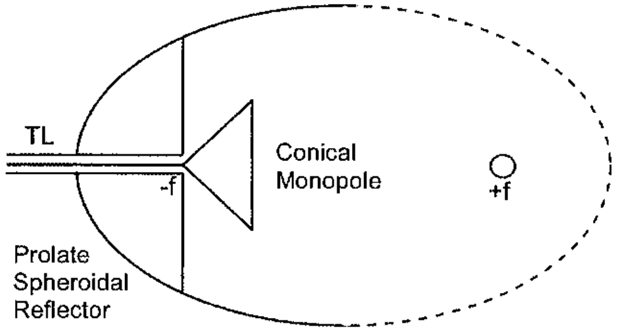

Figure 10: Prolate spheroidal reflector IRA with conical wave launcher.

This thesis focuses on designing and evaluating the focusing characteristics of such an antenna. The next section will discuss the modeling and rationale behind the design of this antenna.

SECTION 3

UWB ANTENNA DESIGN AND MODELING

Based on the survey of the state-of-the-art UWB antennas, the design chosen for this project is a reflector IRA, to allow radiation of high-power sub-nanosecond pulses. Specifically, a reflector IRA with a prolate spheroidal reflector shape will be designed to allow for focusing of high-power, pulsed electric fields at a distance from the edge of the antenna aperture suitable for therapeutic and medical imaging applications. A conical monopole radiator over a ground plane will be used as the wave launcher to provide a fairly frequency-independent radiating element capable of introducing ultra-wideband signals at the first focal point of the prolate spheroidal reflector IRA. To reduce the size of such an antenna, increase the resolution and reduce the transmission and reflection problems associated with delivering electromagnetic waves into tissue, the antenna will be designed for use in a high permittivity medium, specifically water. The success of such an antenna will be judged by an analysis of the electric field radiation distribution. This section will discuss the creation of the model, modeling software, and results.

3.1. Elliptical Geometry

Based on the prolate spheroidal reflector IRA antenna design, two types of antennas will be designed: one with a deep focal point and another with a shallow focal point. To define these focal points the ellipsoidal reflector geometry needs to be evaluated. The geometry of the antenna is symmetric about the major axis; therefore the antenna can be described in a two-dimensional system revolved around the major axis. The equation for an ellipse in a two-dimensional rectangular coordinate system is shown in equation 3.1.1.

$$\frac{(x-h)^2}{a^2} + \frac{(y-k)^2}{b^2} = 1 \qquad (3.1.1)$$

In equation 3.1.1, h, k, a, and b are positive real numbers. The point (h , k) is the two-dimensional origin of the ellipse. The symbol a describes the major axis, and the symbol b describes the minor axis of the ellipse. For the cylindrical coordinate system where the ellipse is centered at the origin, equation 3.1.2 describes the ellipse, where a and b represent the major and minor axis respectively, and (z, r) represents a point on the ellipse in cylindrical coordinates. The geometry of such an ellipse is shown in fig. 11.

$$\frac{z^2}{a^2} + \frac{r^2}{b^2} = 1 \qquad (3.1.2)$$

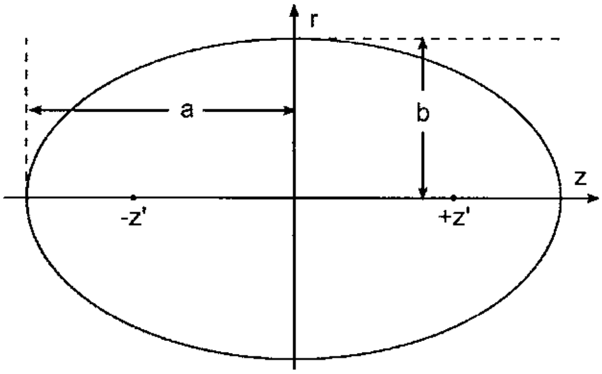

Figure 11: Geometry of an ellipse.

The two focal points of the ellipse are located along the major axis, or in the cylindrical coordinate system, the z axis. The focal points are located such that sum of the distance from one focal point to any point on the ellipse to the second focal point is constant and is always 2a. If the dimensions of the major and minor axes of the ellipse are known, then the focal point can be determined by using the distance formula describing the distance between one focal point (z', 0) and the minor axis intercept (0 , b) which is equal to a. The distance from the origin, (0 , 0), to the foci, (z' , 0), can then be written as in equation 3.1.4. The two foci are then located at (-z' , 0) and (z' , 0).

$$\sqrt{z'^2 + b^2} = a \tag{3.1.3}$$

$$z' = \pm\sqrt{a^2 - b^2} \tag{3.1.4}$$

3.2. Electric Fields at Second Focal Point

The sum of the distance from one focal point to any point on the ellipse to the second focal point is constant. As shown in fig. 12, according to a ray optic interpretation of the radiating signal, when the signal is radiated from the first focal point, the wave will reflect at different parts of the reflector but will all arrive at the same time at the second focal point, since it travels the same distance. While this analysis can hold true for infinite frequencies, the effects of diffraction from the antenna structures are likely to be significant for lower frequencies. This is because at the lower frequencies, the wavelengths of these signals begin to approach dimensions relative in size to antenna structures. To provide a better understanding of the focusing ability of these signals in the near field, modeling will also be used.

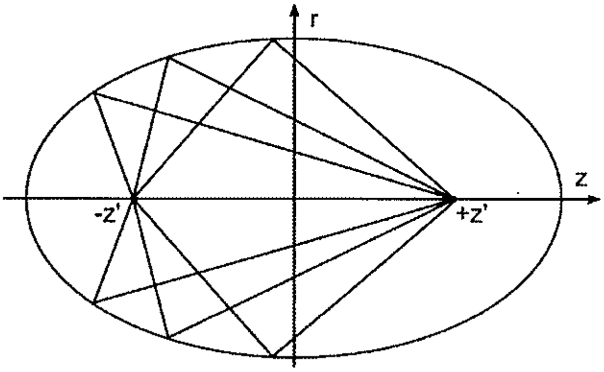

Figure 12: Ray optics interpretation of signal introduced at first focal point.

As a traveling wave moves in one direction, the electromagnetic fields are perpendicular to the direction of travel. The electric and magnetic fields are orthogonal. For the case of our symmetrical prolate spheroidal reflector, the electric field strength of the waves converging at one point is dependent on a cosine effect. Fig. 13 demonstrates this effect. The focused field strength depends on the strength of the traveling electromagnetic wave and the angle of incidence. By resolving the electric field at the focal point into the axial direction and radial direction vectors, it is obvious that the radial electric field will be canceled out by the symmetry of the prolate spheroidal reflector. The electric field in the axial direction is the only vector component that is not canceled by symmetry. From this figure it is evident that as the reflector is closer and closer to the focal point the strength of the electric field will increase as less electric field is canceled in the radial direction. For modeling, then, the field that should be measured is the field in the z-direction.

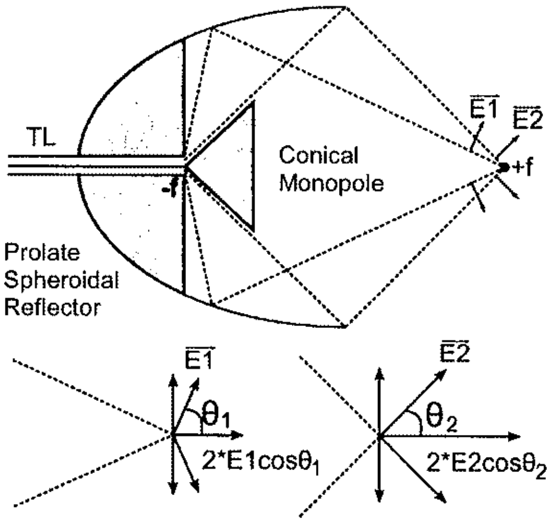

Figure 13: Focused electric field strengths dependent on angle of incidence.

3.3. Model Setup

3.3.1. Modeling Software: MAGIC

The software used to create and evaluate the model is MAGIC, a Finite Difference Time Domain (FDTD) analysis software. The modeling starts by first defining the geometry and electrical properties of the objects in the user-defined configuration. These definitions can then be broken down into a grid containing the electrical properties of each cell.

By using Maxwell's differential equations, it can be shown that the electric field time derivative is dependent on the magnetic field curl in space. Using a time stepping method, an updated value for the electric field value is dependent on the stored values of the previous electric field and magnetic field [56]. This time stepping method is applied to each cell in the grid, where each successive electric field and magnetic field value is stored in the computer and can be turned into usable data through software [57-58]. MAGIC can solve in a three-dimensional or a two-dimensional grid. The coordinate system to be used is the cylindrical coordinate system. The antenna will be revolved about the z direction. Since the antenna is symmetrical about the z axis, the antenna needs to be modeled in only two dimensions.

3.3.2. Model Configuration

Using the defined characteristic equations of the reflector geometry from the above section, along with conical monopole wave launcher dimensions, the MAGIC code is written to display the physical properties of the antenna. The ground plane is placed at the feed focal point. A coaxial transmission line is modeled to feed the signal to the first focal point. A conical monopole is placed at the end of the transmission line at the feed focal point. The transmission line inner conductor, ground plane, conical monopole, and radiator are designated as conductors in the modeling software. A dielectric area with a relative permittivity of 2.1 is placed between the inner conductor of the transmission line and the outer conductor, to simulate a coaxial transmission line. The antenna is then modeled as being placed inside a tank of water with a dielectric permittivity of 81 and negligible conductivity to replicate de-ionized water. To reduce errors in the calculations at the edges of the water dielectric medium, ports with absorption boundary conditions are placed. An example of the model geometry is shown in fig. 14.

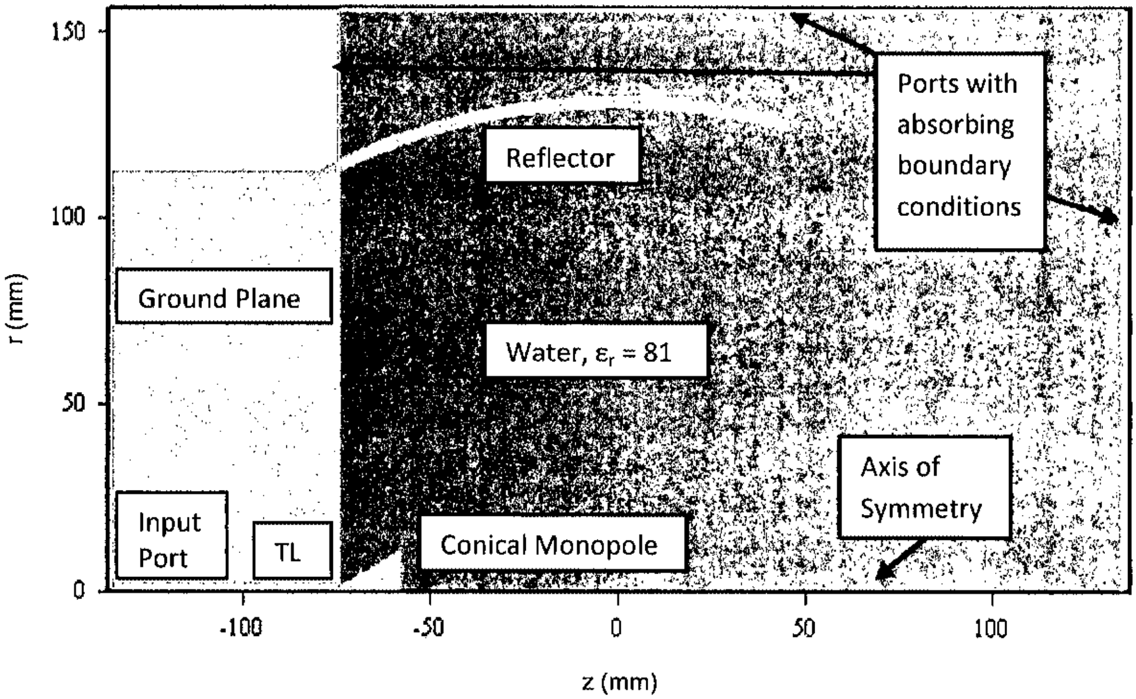

Figure 14: Sample model geometry of proposed antenna submerged in a water medium.

3.3.3. Feed Signal

Once that geometry is generated, a signal can be fed to the transmission line input of the modeled antenna. The important property of the simulated pulse is the rise time. To be able to compare the expected results against experimental results, the simulated pulse is limited by the available pulse generator. The device used to evaluate the experimental antenna is a desktop FID G2039 pulse generator, which outputs a pulse with maximum 5 kilovolt amplitude, 250 nanosecond pulse width, and a rise time of 200 picoseconds. Therefore, in the model a similar high-voltage pulsed signal is used, rather than the ideal step function, to generate the ultra-wideband signal. Fig. 15 shows the signal that is applied at the transmission line feed. Since the system is not balanced, there is a reflection, shown following the initial pulse, with an opposite polarity. The impedance of this antenna is determined by the conical radiator dimensions and the electrical properties of the water.

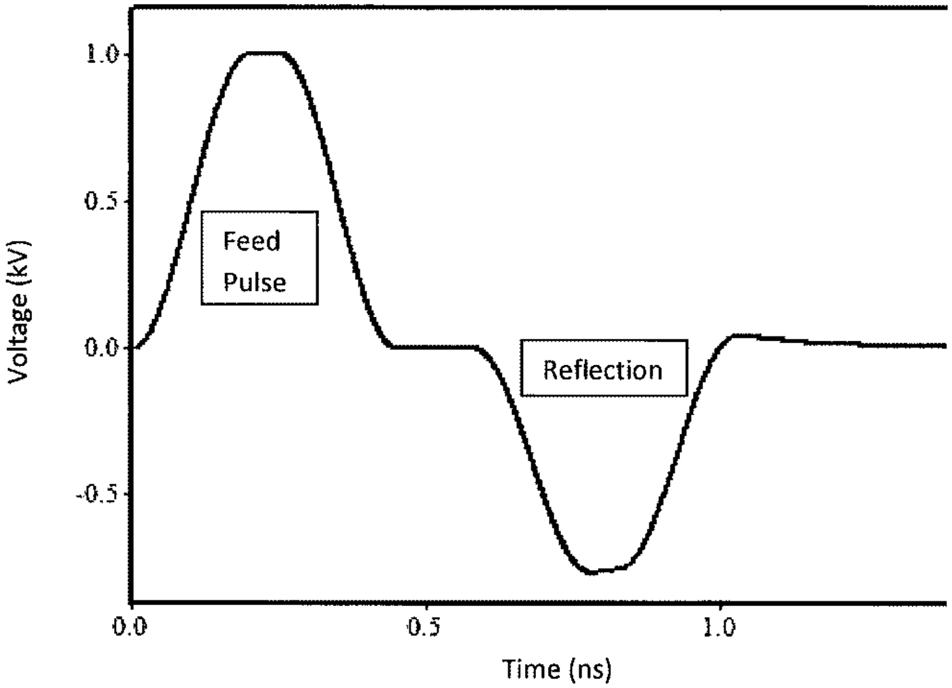

Figure 15: Input pulsed signal.

The antenna may also be interesting for study as a localized tissue heating device. Localized heating of cancerous tissue may also be possible using this antenna with microwave frequencies, leading to hyperthermia or ablation of the target tissue. This is often accomplished using RF or microwave applicators that may penetrate only as far as 3-4 centimeters [59-60]. Therefore, narrowband sinusoidal waves with frequencies centered at 900 MHz and 1500 MHz will also be modeled.

3.4. Model Analysis

The antenna will be modeled with various configurations to achieve some understanding of the field behavior inside the reflector. This will provide information to determine a design for the real antennas to be built and tested.

3.4.1. Field Measurements

Fig. 16 shows a contour plot of the electric fields of a sample geometry as the signal is radiated. From this you can see diffraction occurring at the edge of the conical radiator and reflector. As the field is focused by the reflector, energy that was diffracted is not focused and exits the antenna. This may affect the focusing ability of the antenna.

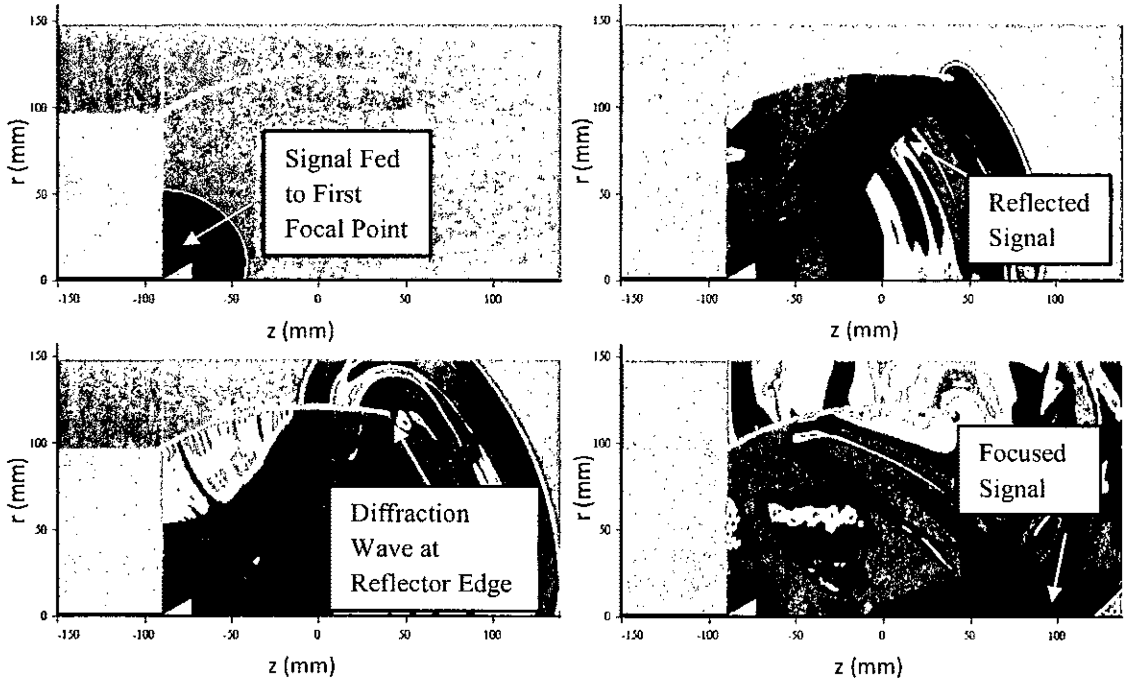

Figure 16: Electric field contour plot of sample geometry shows diffraction and focusing.

Fig. 17 displays the measured electric field where the signal is focused. From this figure, there first appears to be a small pulse, called the pre-pulse, which comes from the diffraction at the cone edge. Then there is the actual ultra-wideband impulse generated by the radiation of the pulsed signal. Following the ultra wideband impulse there are many reflections that can be attributed to the non-ideal shape of the feed signal and the diffraction at the cone and reflector edges. The important information here is the first impulse following the pre-pulse; it will be used to measure the electric field distribution of the antenna.

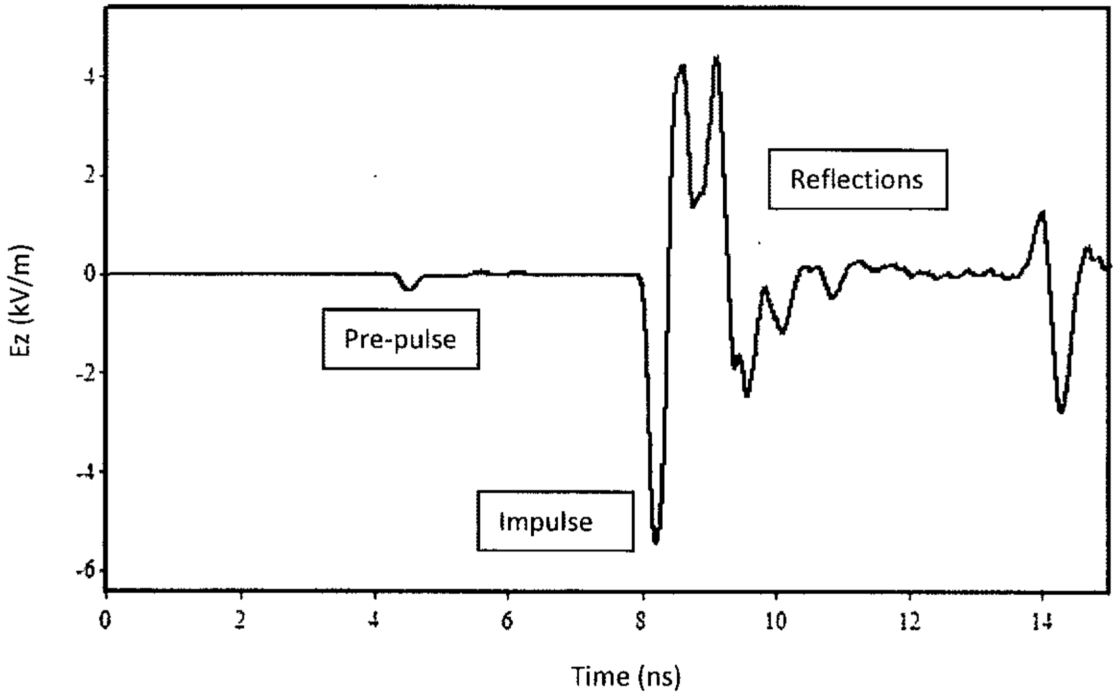

Figure 17: Electric field measured at focal point of sample antenna.

3.4.2. Electric Field Dependence on Major and Minor Axis of Reflector

The deep focusing antenna submerged in water, was modeled for various ratios of the major axis, a, to the minor axis, b. This a/b ratio can be used to adjust the focal point of the antenna. Geometry is shown below in fig. 18, for a deep focusing antenna based on a high a/b ratio. Fig. 19 shows the geometry of a shallow focusing antenna where the a/b ratio is approaching 1. The ground plane of the conical monopole is placed at the left focal point. The light gray section describes a conducting material, in this case aluminum; the white describes the PTFE part of a coaxial cable that is placed between the inner and outer conductor; and the dark gray represents the portion of the grid that relates to the water in which the antenna is submerged.

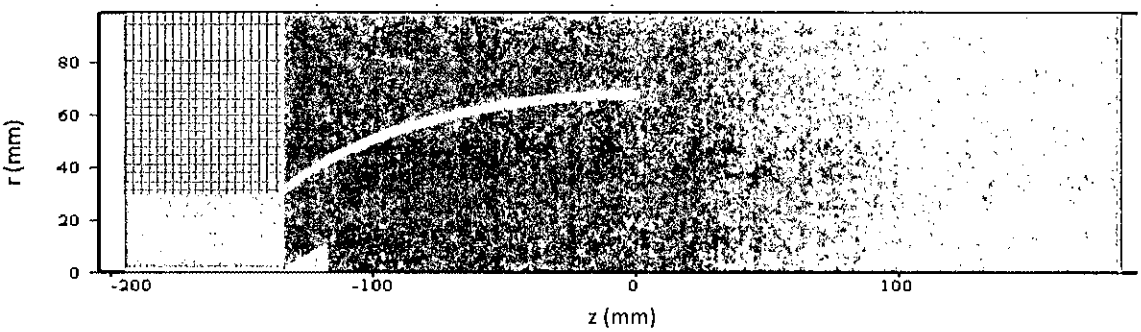

Figure 18: Deep focusing prolate spheroidal reflector IRA model.

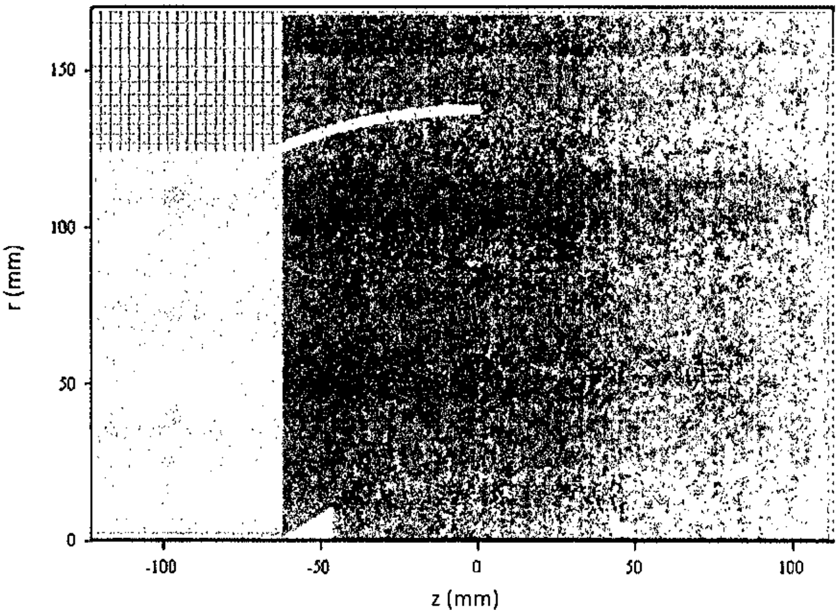

Figure 19: Shallow focusing prolate spheroidal reflector IRA model.

Table 1 compares some of the focusing characteristics based on the a/b ratio. Fig. 20 shows the electric field distribution for the varied a/b ratios. The horizontal axis of the field distribution is adjusted to line up the geometric focal point of each a/b ratio. The geometric focal point is calculated from equation 3.1.4. According to the results the focal point is shifted closer to the first focal point than predicted for higher a/b ratios. The sharpness of the electric field distribution is also reduced as the a/b ratio is increased. Higher a/b ratios may allow for deeper focusing of ultra-wideband impulses. Even though the focal point modeled is not at the optical focal point, these antenna designs may still allow for a deep focusing (large a/b ratio) and shallow focusing (small a/b ratio) antenna.

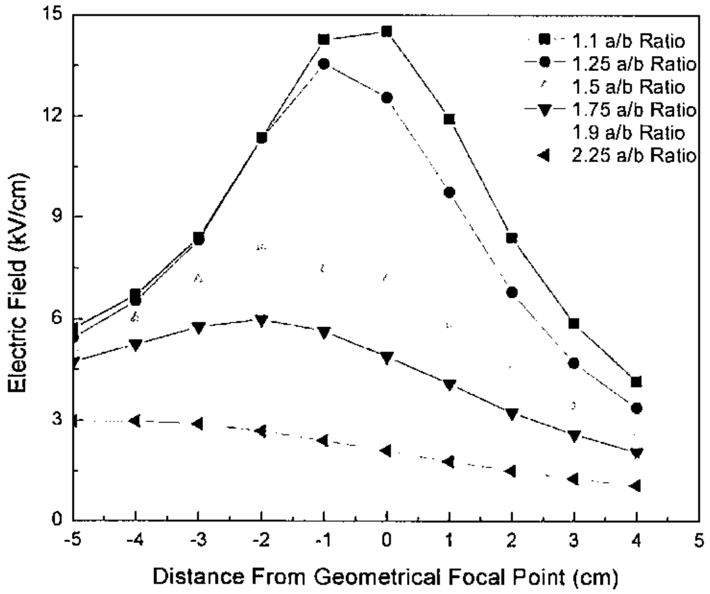

Figure 20: Electric field distribution for varying a/b ratios. Origin is geometric focal point for that a/b ratio.

Table 1: Comparison of focusing characteristics of various a/b ratios.

a/b ratio	Geometrical Focal Point	Modeled Focal Point	Maximum Electric Field
2.25	(± 13.5 cm, 0 cm)	(± 9.4 cm, 0 cm)	2.98 kV/cm
1.9	(± 12.7 cm, 0 cm)	(± 9.8 cm, 0 cm)	4.78 kV/cm
1.75	(± 12.4 cm, 0 cm)	(± 10.4 cm, 0 cm)	6.00 kV/cm
1.5	(± 11.2 cm, 0 cm)	(± 9.2 cm, 0 cm)	8.13 kV/cm
1.25	(± 9.0 cm, 0 cm)	(± 8.0 cm, 0 cm)	13.56 kV/cm
1.07	(± 6.3 cm, 0 cm)	(± 6.3 cm, 0 cm)	14.52 kV/cm

3.4.3. Electric Field Dependence on Surface Area of Reflector

Another variable to look at is the surface area. If the a/b ratio is kept the same, by adjusting the surface area of the reflector, the depth of the focal point can be adjusted. Fig. 21 shows the electric field distributions of different reflector surface areas, where the distance from the edge of the reflector to the focal point is adjusted. The results suggest that by increasing the surface area the electric field intensity also increases, as does the sharpness of the focus. However, as the surface area increases, the edge of the reflector gets closer to the focus, and the shallower the depth of focusing becomes. Also, as the surface area is reduced the focus spot amplitude appears to decrease and as with the adjustment of the a/b ratio, the focal point moves away from the geometric focal point and closer to the reflector edge. However, for a deep focusing antenna, the negative effects of reducing the surface area and increasing the a/b ratio will have to be conceded to a degree as long as focusing can be achieved.

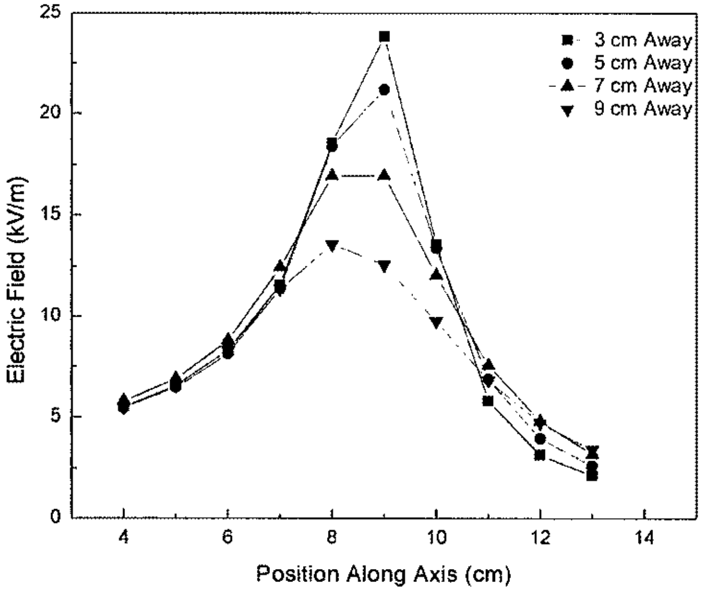

Figure 21: Electric field distribution for varying reflector surface areas.

3.4.4. Electric Field Dependence on Conical Radiator Dimensions

Another area of interest is the optimization of the conical radiator. By adjusting the cone length, L_C, described in fig. 22, the intensity of the electric fields may be changed. Since the UWB pulse contains a wide range of frequencies, this effect should occur because, as previously stated, the radiator will limit the radiation of lower frequency signals.

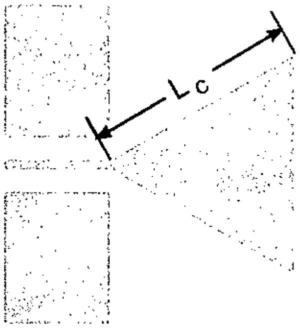

Figure 22: Conical monopole over a ground plane radiator used to launch UWB signal.

The length of L_C was varied with reference to the pulse width of the UWB pulse. The resulting waveforms are located below in fig. 23. From these results it can be shown that as long as the radiator is longer than 1 pulse width of the signal then the conical monopole over a ground plane is a good radiator for UWB pulses.

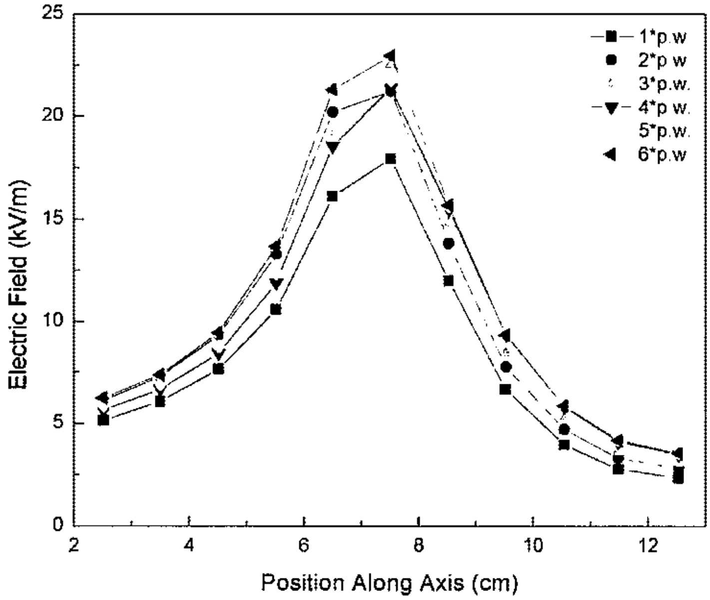

Figure 23: Electric field distribution for varying lengths of cone length, L_C.

3.5. Simulation of Actual Antennas

3.5.1. Design Parameters

Based on the modeling results and the goals of the thesis, the designs were chosen to develop a deep focusing antenna and a shallow focusing antenna. The deep focusing antenna may not be able to achieve as high electric fields as the shallow focusing antenna based on the reflector design. The deep focusing reflector used for this thesis, acquired from the Melles Griot company, has an a/b ratio of 1.9, and the geometric focal point of this reflector is 15.5 centimeters from the edge of the reflector. However, according to the optimization results the actual focal point may be closer to the reflector edge, which will decrease the depth of the antenna. The shallow focusing antenna will have an a/b ratio of 1.25, and the reflector edge will be placed 5 centimeters from the geometrically calculated focal point. This provides focusing that is equivalent to that of some of the deepest applicators used in microwave heating and ablation. The dimensions of the two antennas are presented in table 2.

Table 2: Dimensions of the deep and shallow focusing antennas.

Antenna	Cone Length	a/b Ratio	Focusing Depth to Geometric Focal Point
Deep Focusing	3 cm	1.9	15.5 cm
Shallow Focusing	3 cm	1.25	5 cm

3.5.2. UWB Fed Simulation Results for Deep Focusing Antenna

The following two figures show the electric field distribution along the z-axis and radial axis for the UWB feed signal for the deep focusing reflector IRA. These figures show that the antenna achieves some focusing effect. The axial field was measured first, then the radial field, from the center outward, fixed in the z direction at what appeared to be the focal point along the axis. In the z-direction, the electric field magnitude is higher around one point, as shown in fig. 24. The pulse does not appear to be focused at the geometric calculated focal point, but rather much closer to the reflector edge as predicted.

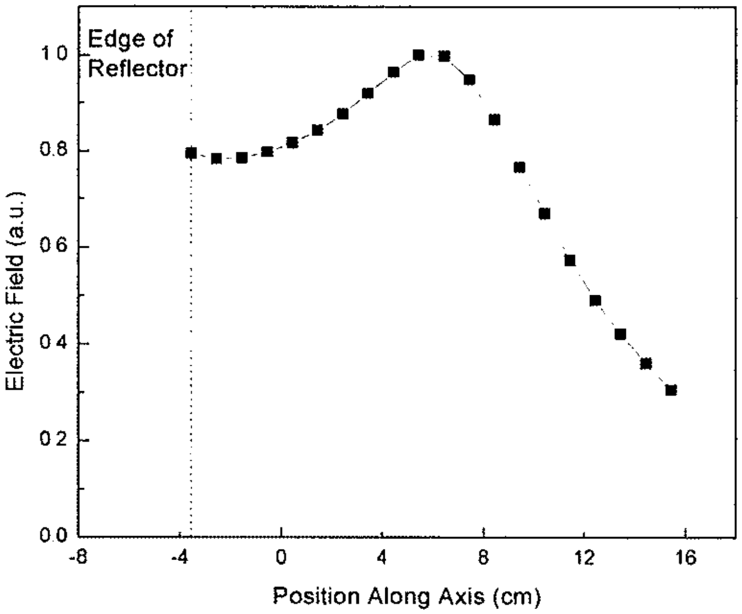

Figure 24: Simulated electric field distribution for deep focus prolate spheroidal reflector antenna in the axial direction.

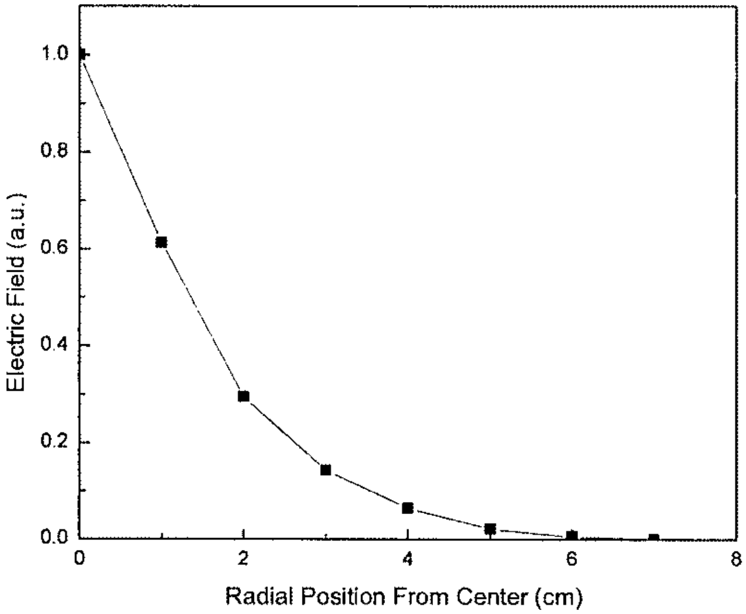

Figure 25: Simulated electric field distribution for deep focus prolate spheroidal reflector antenna in the radial direction.

Fig. 25, the radial distribution of the electric field, makes clear that the signal is much higher toward the axis, or center. From these two figures the focusing spot size dimensions of the antenna can be estimated to be about 4.5 centimeters axially by about 3 centimeters wide.

3.5.3. UWB Fed Simulation Results for Shallow Focusing Antenna

Fig. 26 and 27 show the electric field distribution in the axial and radial directions for the shallow focusing reflector IRA. Again it appears that focusing is evident here, where the electric field appears much higher as it approaches the focal point. As predicted, based on the previous modeling, the signal is much sharper and focused at the correct geometric focal point.

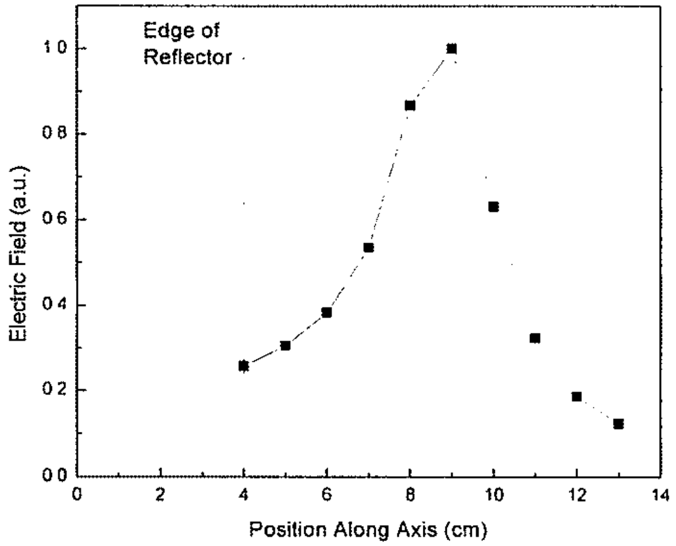

Figure 26: Simulated electric field distribution of the impulse for the shallow focus prolate spheroidal reflector antenna in the axial direction.

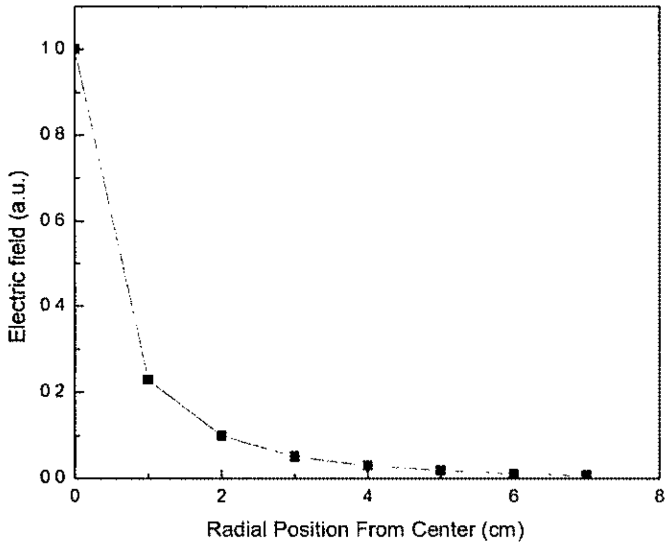

Figure 27: Simulated electric field distribution of the impulse for the shallow focus prolate spheroidal reflector antenna in the radial direction.

The radial distribution does show that there is focusing toward the axis. Based on the modeling results, the spot size for the pulsed signal is about 3 centimeters in the axial direction by about 1.5 centimeters wide. The focusing with this antenna provides a much better resolution than the deep focusing antenna. However, the focused electric fields are only 5 centimeters deep.

3.5.4. Narrowband Fed Simulation Results for Deep Focusing Antenna

The electric field distribution of two specific sinusoidal signals with frequencies of 900 MHz and 1500 MHz will also be modeled. To evaluate the electric field distribution, peak-to-peak voltage measurements will be made. The next figure shows the electric field distribution of the 900 MHz and 1500 MHz sinusoidal signals in the axial direction and the radial direction. As with the UWB-fed signal, the electric field is not focused at the optical second focal point but is closer to the edge of the deep focusing reflector, which was to be expected.

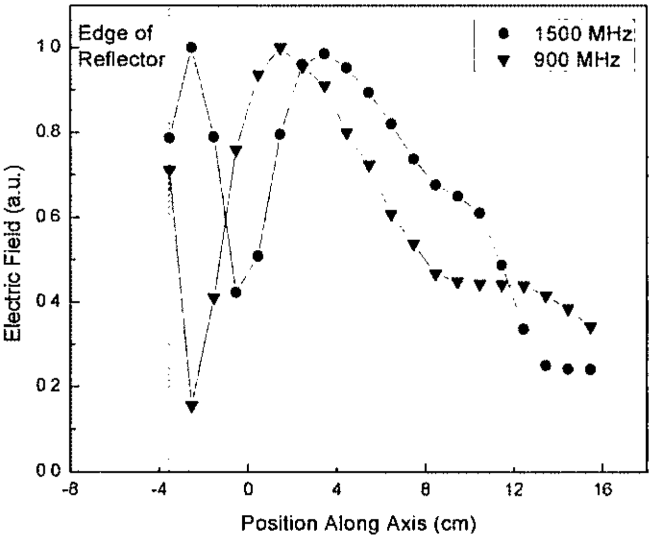

Figure 28: Simulated electric field distribution at narrowband frequencies for deep focus prolate spheroidal reflector antenna in the axial direction.

In the axial direction for a 900 MHz sinusoidal feed signal, the electric field magnitude is focused about 5 centimeters from the edge of the reflector, much closer than the optical focal point. For a 1500 MHz sinusoidal feed signal, the electric field distribution in the axial direction shows that the focal point is located about 7 centimeters from the edge. Once again, this is much closer than the expected focal point. The next figure shows the radial distribution of the electric field for the narrowband signals. The radial measurement is fixed in the z-direction at the position of the axial focusing for each narrowband frequency.

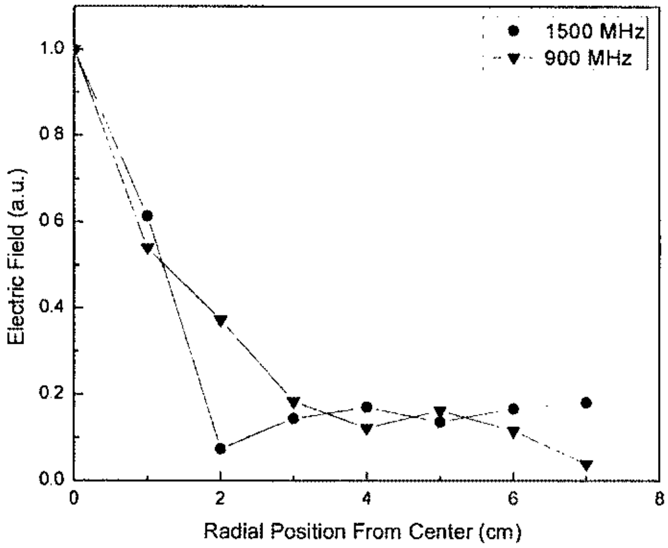

Figure 29: Simulated electric field distribution at narrowband frequencies for deep focus prolate spheroidal reflector antenna in the radial direction.

The radial distribution for the narrowband signals shows a higher field toward the z-axis. The modeling results for the 900 MHz signal for this antenna show that the focusing is located about 5 centimeters from the end of the reflector. The spot size at this focal point for 900 MHz is about 6.5 centimeters long by about 3.5 centimeters wide. The modeling results for the 1500 MHz signal for this antenna show that the focusing is located about 7 centimeters from the end of the reflector. The spot size for the 1500 MHz frequency at this focal point is about 5 centimeters in the axial direction by about 2.5 centimeters wide.

3.5.5. Narrowband Fed Simulation Results for Shallow Focusing Antenna

Similarly, narrowband signals were evaluated for the shallow focusing prolate spheroidal reflector IRA. The signals were introduced into the antenna to evaluate the electric field distribution of the antenna at those frequencies. Fig. 30 displays the corresponding electric field distributions.

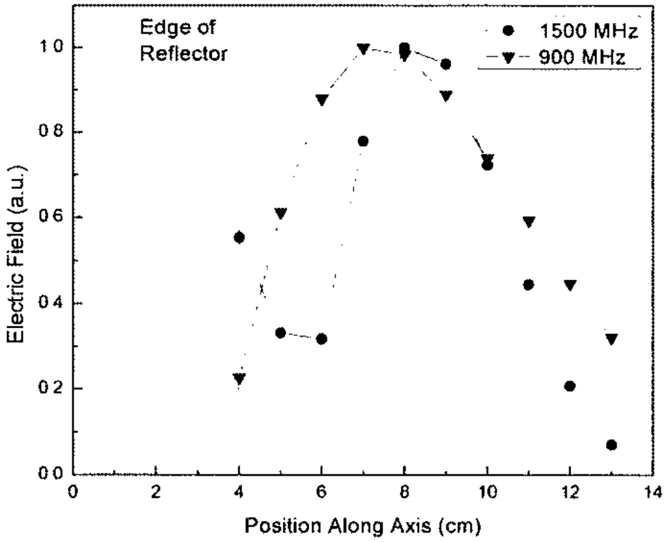

Figure 30: Simulated electric field distribution of the narrowband signals for the shallow focus prolate spheroidal reflector antenna in the axial direction.

In fig. 30, the 900 MHz signal appears to focus about 3 centimeters from the edge of the reflector. The observed focal point for the 1500 MHz signal is shown to be closer to the geometric focal point than the 900 MHz signal, whose observed focal point is about 4 centimeters from the edge of the reflector. Fig. 31 shows the radial distribution of the electric field for the narrowband sinusoidal signals.

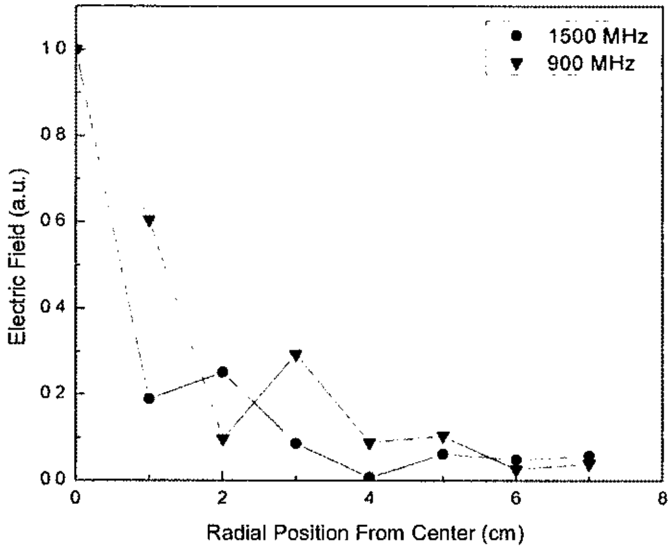

Figure 31: Simulated electric field distribution of the narrowband signals for the shallow focus prolate spheroidal reflector antenna in the radial direction.

Again the radial distribution shows focusing toward the z-axis. The focus spot size of this antenna for the 900 MHz signal is about 6 centimeters along the z-direction and about 3 centimeters wide. The focus spot size for a 1500 MHz signal in this shallow focusing antenna is about 4 centimeters in the axial direction by 1.5 centimeters wide.

3.6. Summary of Modeling Results

The following tables 3 and 4 compare the predicted values to the results from the modeling for the deep and shallow focusing reflector respectively.

Table 3: Modeling comparison for the deep focusing prolate spheroidal reflector IRA.

	Feed Signal		
	Pulse	900 MHz	1500 MHz
Optical Focal Point	(12 cm, 0 cm)	(12 cm, 0 cm)	(12 cm, 0 cm)
Modeled Maxima	(7 cm, 0 cm)	(2 cm, 0 cm)	(4 cm, 0 cm)
Modeled Spot Size	4.5 cm x 3 cm	6.5 cm x 3.5 cm	5 cm x 2.5 cm

Table 4: Modeling comparison for the shallow focusing prolate spheroidal reflector IRA.

	Pulse	900 MHz	1500 MHz
Optical Focal Point	(9 cm, 0 cm)	(9 cm, 0 cm)	(9 cm, 0 cm)
Modeled Maxima	(9 cm, 0 cm)	(7 cm, 0 cm)	(8 cm, 0 cm)
Modeled Spot Size	3 cm x 1.5 cm	6 cm x 3 cm	4 cm x 1.5 cm

These results suggest that the shallow focusing prolate spheroidal reflector IRA may provide sharper focusing of the electromagnetic waves at the modeled focal point. The deep focusing reflector IRA may be able to deliver focused electromagnetic signals still twice as deep as the shallow focusing reflector IRA. While the focusing may not be as sharp as the previous case, it can be defined alternatively by a certain range for the electric field. For example, if the electric field strength that can be effective is only of intensities above 80 percent of the maximum intensity, then the focusing ability of that antenna will pertain to the electric field intensities that match that criterion.

The modeled focal point may have been closer because of the diffraction waves generated at the edge of the conical radiator and the edge of the reflector. This effect appears to have affected the narrowband frequencies of the deep focusing reflector IRA in the most negative way. Regardless, focusing does appear to occur in all cases, even if not located at the optical focal point. Both the deep focusing and shallow focusing prolate spheroidal reflector IRAs will be designed, manufactured, and evaluated for this thesis, as the next section describes.

SECTION 4

EXPERIMENTAL

4.1. Fabrication of the Deep Focusing Reflector IRA

For the deep focusing reflector IRA, as previously mentioned the reflector from Melles Griot was used. The dimensions of the reflector were used in a three-dimensional CAD software to aid in the design of the antenna. The ground plane of the coaxially fed conical monopole had to be placed at the feed focal point of the reflector. To do this the equation for the ellipse was used and the z-axis value for the feed focal point was substituted into the equation to find the radial value, which describe the radial width of the ellipse at the focal point. This value was then set as the radius of the circular ground plane. The ground plane was then given a sharp edge so that only the edge at that radius came into contact with the reflector and would place the ground plate at precisely the correct focal point.

To attach the coaxial input to the ground plane, a panel mount with an extended dielectric (Pasternack Enterprises model number PE4444) was used. The center hole of the ground plane was drilled so that it fit snugly to the dielectric and acted electrically as a continuation of the coaxial transmission line feed. The ground plane was about a quarter inch thick, to allow the panel mount to be screwed into it. The dielectric of the panel mount was trimmed back to make it flush with the ground plane. Then the exposed inner conductor was threaded to allow for the conical radiator to be fastened on to it at the focal feed point.

The conical radiator was machined from aluminum round stock, with an angle of 30 degrees. The length of the conical radiator defines the lower bandwidth limit of the radiator. This radiator had a through hole drilled in the tip of the cone. The cone was attached to the inner conductor by a threaded lock that screws onto the threaded inner conductor.

The prolate spheroidal reflector had a hole in one end that allowed for the cable to be fed into the reflector. To fix the ground plane at the correct position the reflector, a piece of round stock was hollowed out to allow the cable's N-type connector to slide through easily. On the end of the N-type connector are two flat sections, one on each side. A hole was drilled through the tube and threaded so that a set screw could be put in to secure the cable. To place the ground plane in the correct position, the outside of the tube holding the cable was threaded. Then a lock nut was fabricated that could be screwed onto the tube. This fastens the ground plane in place by pulling it to the correct position inside the reflector.

To measure the electric field distribution, the antenna was connected to a rail system. Another piece of aluminum round stock was threaded to fit on the end of the tube holding the cable. This attachment piece has a threaded hole to allow for the attachment of an optical post to attach the antenna to \ the rail above, when suspended in media. The constructed version of the conical monopole wave launcher and hardware arranged to secure the ground plane at the correct position is shown in fig. 32.

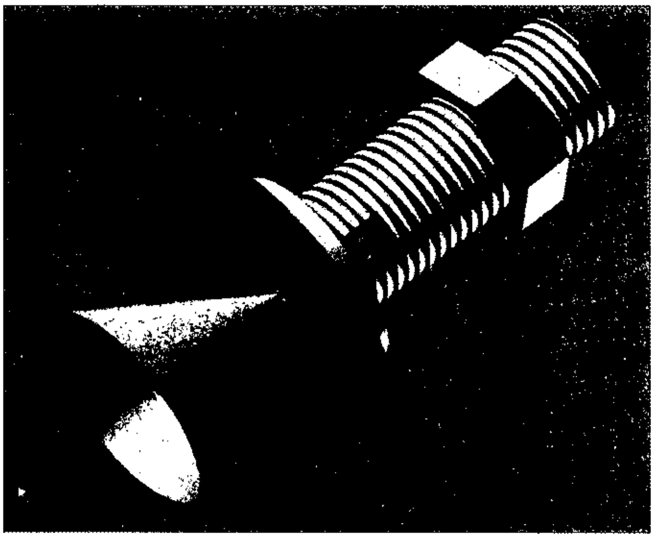

Figure 32: Conical monopole over a ground plane design for deep focusing prolate spheroidal reflector IRA.

Fig. 33 shows the antenna with the secure conical monopole in place in the CAD drawing as well as the fully manufactured antenna attached to the rail system. The majority of the parts were made of aluminum to reduce the weight of the antenna.

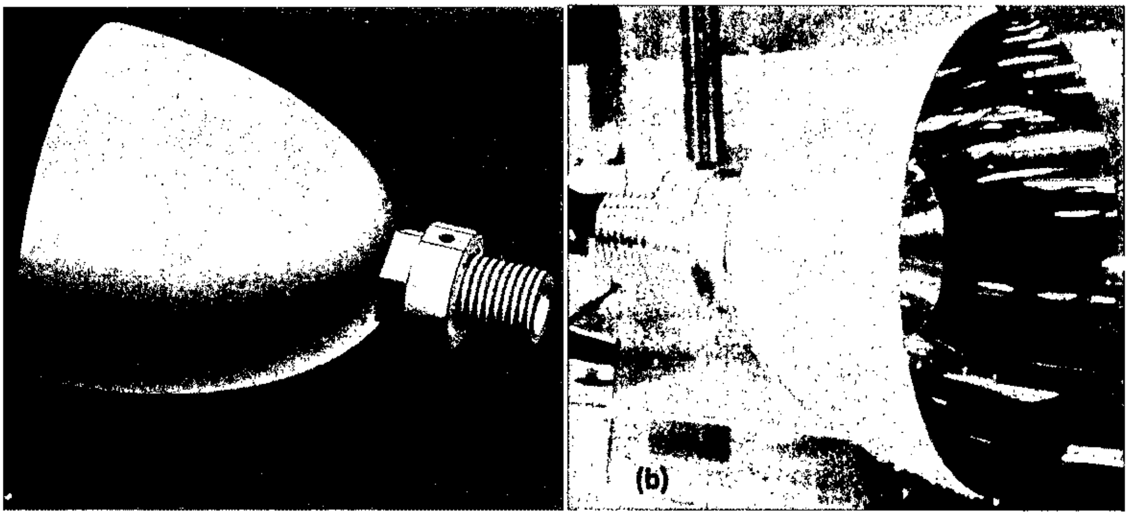

Figure 33: (a) CAD drawing and (b) experimental deep focusing prolate spheroidal reflector IRA.

4.2. Fabrication of the Shallow Focusing Reflector IRA

The reflector for the shallow focusing antenna was designed using the CAD software. Based on the modeled dimensions of the reflector, an aluminum sheet metal model was fabricated by a prototyping company. To attach the ground plane, four tabs were placed around the outside edge of the reflector. This design was used to secure the ground plane at the first focal point. The ground plane is similar to the one used for the first antenna, although with a much larger diameter. A similar hole is in the center of the aluminum plate of the ground plane for the panel mount component to fit into. The panel mount attachment is secured to the ground plane the same way as for the deep focusing reflector. The top of the ground plane has a threaded hole to allow it to connect to an optical post. The post can then be attached to a rail system to allow for evaluation of the electric field distribution. A coaxial feed cable with a type-N connector is attached to the panel mount to launch the signal. The completed CAD drawing of the antenna with the reflector and ground plane is shown in fig. 34, along with the completed antenna itself.

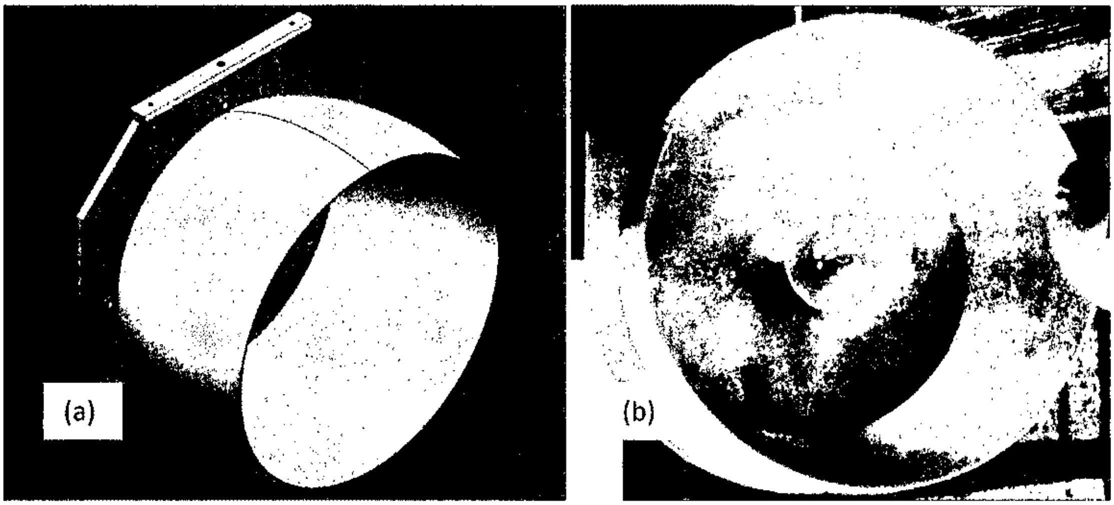

Figure 34: (a) CAD drawing and (b) experimental fabrication of shallow focusing prolate spheroidal reflector IRA.

4.3. Experimental Setup and Diagnostics

A 12-gallon tank was filled with de-ionized water. The conductivity of the water was measured to be about 3 microsiemens. An optical rail was fixed above the water tank, where the antenna would be submerged. The antenna was then connected to the rail by an optical post. The probe was connected to the rail as well on a sliding optical stage. This optical stage slid along the rail to take measurements along the axial direction. Another perpendicular rail was added to allow measurement of the field along the radial direction as well. The data was collected starting at the edge of the antenna reflector and then taking measurements moving away from the antenna in the axial direction. Then if focusing was observed, radial measurements were made. These measurements were taken by fixing the axial sliding rail at the observed focal point, then moving the radial sliding rail away from the axis. Fig. 35 shows the experimental setup.

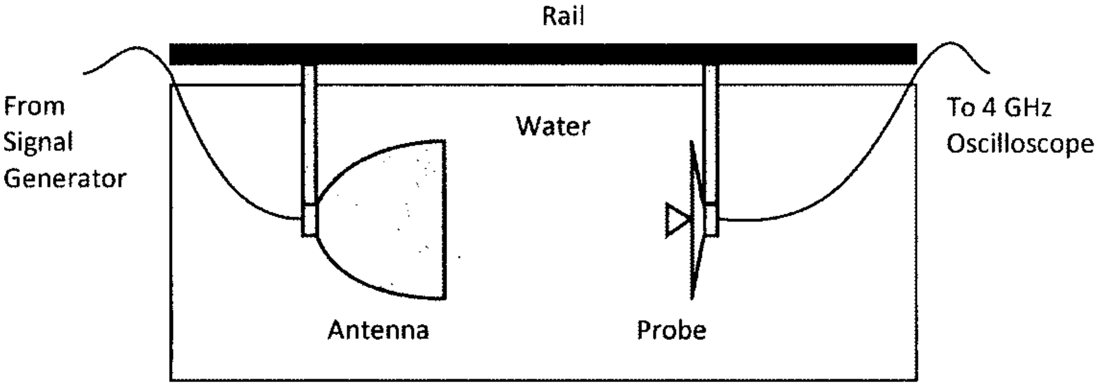

Figure 35: Test setup of submerged antenna and probe on rail system.

To deliver the ultra-fast UWB pulse, an FID GmbH picosecond pulse generator was used. This desktop pulse generator was manufactured by FID Technologies. This adjustable pulse generator delivers a maximum 5 kilovolt pulse that was measured to have a pulse width of 240 picoseconds, and a rise time of about 200 picoseconds. The FID pulse generator and the high voltage output signal are shown in fig. 36. Narrow band wave focusing was also evaluated using the output of a network analyzer. Two different 10 decibel signals were used, one transmitting with a center frequency of 900 MHz, and the other with a center frequency of 1500 MHz.

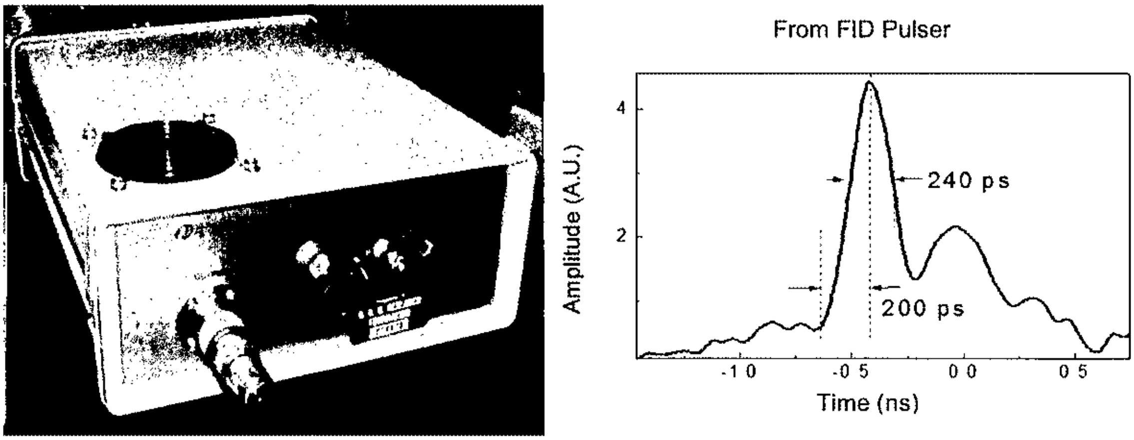

Figure 36: FID GmBh pulse generator and output pulse.

The probe used to measure the signal is a conical monopole over a ground plane, similar to the wave launcher for the signal, seen in fig. 37. This probe was connected to the rail using another optical rod connected to a sliding optical stage. The orientation of this probe will allow for measurement of the fields in the axial, or z-direction. This probe is designed to work on the axis. When measurements are taken for the radial distribution, the probe may collect more than just the fields measured in the z-direction. This probe acts similar to a D-dot probe manufactured by Prodyne. The voltage output of the probe is given in the equation in 4.3.1, where R is the sensor characteristic load impedance of the probe, A is the sensor equivalent area, and D is the magnitude of the electric displacement vector. The definition of the permittivity is given in equation 4.3.2. From these two equations it is obvious that to get the electric field measurement from the probe, the measured voltage needs to be integrated [61]. The probe was connected to a 4 GHz, 20 giga-sample per second digital phosphor oscilloscope. The Tektronix model TDS 7404 is used to capture all the data for this experiment. To measure the pulse, two 20 decibel attenuators were used to avoid damaging the sensitive oscilloscope.

$$V = RA\frac{dD}{dt} \tag{4.3.1}$$

$$D = \varepsilon E \tag{4.3.2}$$

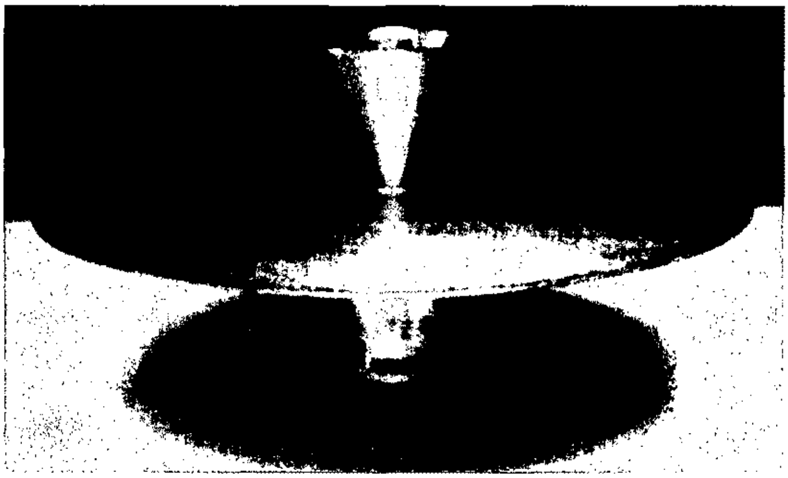

Figure 37: Conical monopole probe.

To eliminate the noise inherent to the pulses, 30 waveforms were averaged when collecting the data. Each waveform was saved into a waveform data file. The data was then be processed and analyzed by looking at the impulse of the pulsed signal, and the peak-to-peak voltage of the narrowband sinusoidal wave. To analyze the UWB impulse, the data needs to be integrated with respect to time, since as in equation 4.3.1 the probe's voltage is a differentiation of the electric field. This integrated impulse data can then be used to determine the electric field distribution of the antennas. The process for collecting the data is shown in fig. 38. The results of the experiment are presented in the next section.

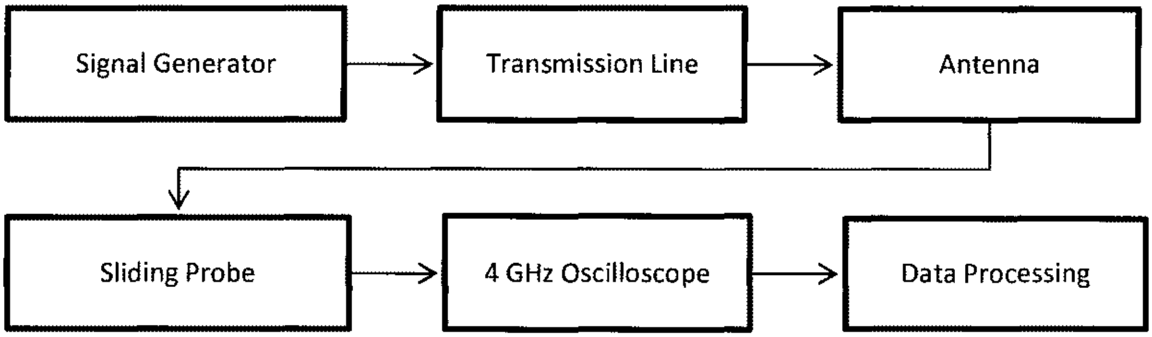

Figure 38: Process to capture and analyze the field behavior of the antennas.

SECTION 5

EXPERIMENTAL RESULTS

5.1 Measured UWB Waveform on Axis

Fig. 39 shows the waveform measured by the probe when an ultra-wideband impulse was transmitted by the shallow focusing antenna. As stated previously, the probe records a differentiation of the electric field, therefore integration of the measured signal is required. Fig. 40 shows the integration of the waveform signal. The first small peak of the measured waveform is the pre-pulse, resulting from a diffraction wave that is generated at the edge of the conical radiator and reaches the probe before the wave that arrives by way of the reflector. As was shown in the simulation, the pre-pulse has the same polarity as the impulse. Therefore, the first peak that is measured after the pre-pulse will be the impulse. The integrated waveform data will show the positive pre-pulse as well as the positive impulse. This peak is measured along the axis to look for focusing.

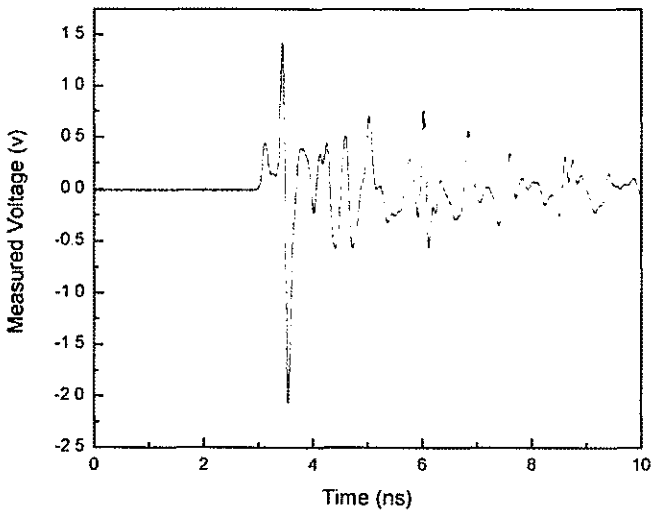

Figure 39: Measured voltage from probe at a point along the z-axis of the shallow focusing antenna.

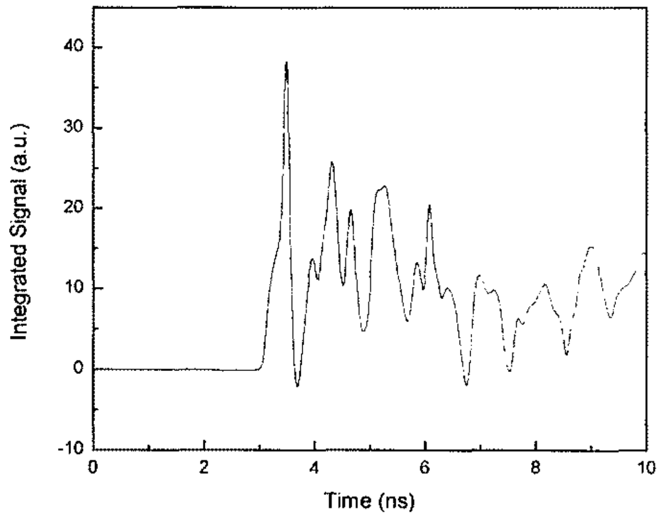

Figure 40: Integrated voltage from probe at a point along the z-axis of the shallow focusing antenna.

5.2. Electric Field Distribution for Deep Focusing Antenna Fed with UWB Signals

The measured waveforms were analyzed to look for focusing near the expected focal point based on the simulation of the antenna. The following set of results is from the first antenna that focuses farther away. Fig. 41 shows the distribution of the voltage amplitude of the impulse along the z-axis. Here it appears, when compared to the modeled results, that the focal point is much closer to the edge of the reflector than expected. The focusing also does not appear to be as sharp as it was expected to be based on the modeling. Fig. 41 also shows the distribution of the integration of that signal along the z-axis direction, which is the distribution of the electric field. From this distribution it appears that the maximum value of the distribution is close to the edge of the reflector.

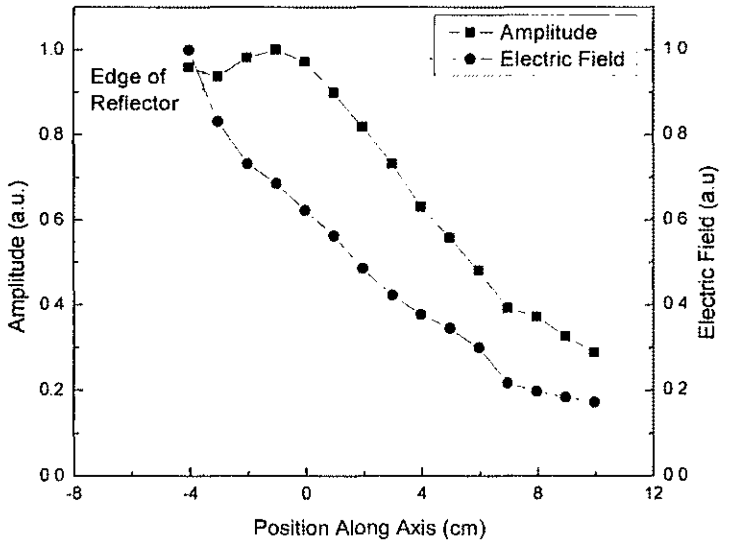

Figure 41: Electric field distribution of the impulse for the deep focus prolate spheroidal reflector antenna in the axial direction.

In the radial direction, field measurements were made at what appeared to be the focal point at 2.5 centimeters away from the edge of the reflector. From these results we can see that the signal is focused at the axis. The decrease in the signal strength as the probe is moved outward is very sharp. Fig. 42 shows the radial distribution of the voltage amplitude measurements before the signal is integrated. Fig. 42 also shows the electric field distribution of the integrated impulse in the radial direction. Here there also appears to be focusing toward the z-direction axis. The width is about the same.

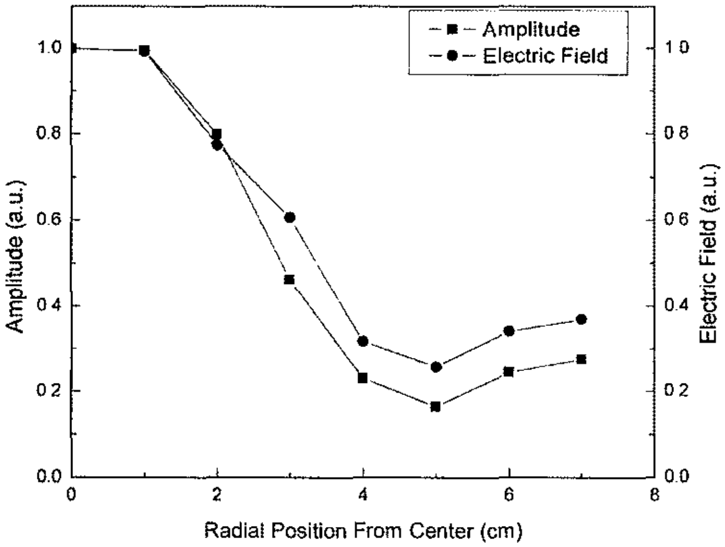

Figure 42: Electric field distribution of the impulse for the deep focus prolate spheroidal reflector antenna in the radial direction.

Based on these results of the integrated signal, a focus spot cannot be observed for this antenna when fed with an ultra-wideband signal. The voltage amplitude distribution suggested that there may be focusing closer to the reflector than modeled, located only about 2.5 centimeters away from the reflector edge. However, after integrating the measured signal to solve for the electric field, focusing is not observed.

5.3. Electric Field Distribution for Shallow Focusing Antenna Fed with UWB Signals

The next set of experimental results is for the shallow focusing prolate spheroidal reflector IRA. The measured waveforms were analyzed to look for focusing near the expected focal point based on the simulation of the antenna. The following experimental result in fig. 43 displays the distribution of the measured voltage amplitude along the z-axis. Here it is very hard to observe focusing. The voltage distribution seems to level off before decreasing. The region in which it levels off is much closer than where the modeling results indicate should be a local maximum. Fig. 43 also shows the distribution along the z-axis direction of the electric field. Again the electric field is calculated by integrating the voltage amplitude measurements. From this figure the maximum value of the distribution is located at the reflector edge.

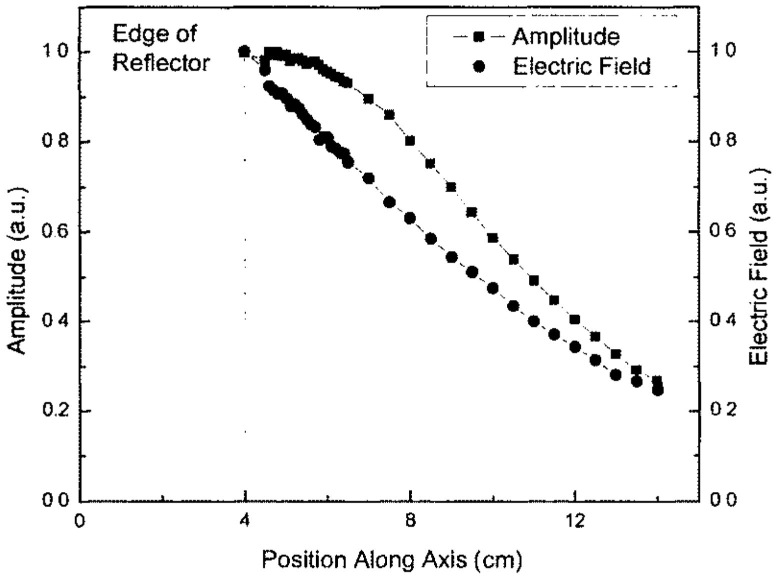

Figure 43: Electric field distribution of the impulse for the shallow focus prolate spheroidal reflector antenna in the axial direction.

In the radial direction, voltage amplitude measurements were made where the voltage amplitude signal leveled off at 1.5 centimeters away from the edge of the reflector. From these radial results it is evident that the pulsed signal is stronger at the axis. The radial width of the distribution is wider than expected from the modeling results. Fig. 44 shows the radial distribution of the voltage amplitude measurements before the signal is integrated. Fig. 44 also shows the electric field distribution of the integrated pulsed signal measured in the radial direction. Here the radial width of the distribution appears to be twice as wide.

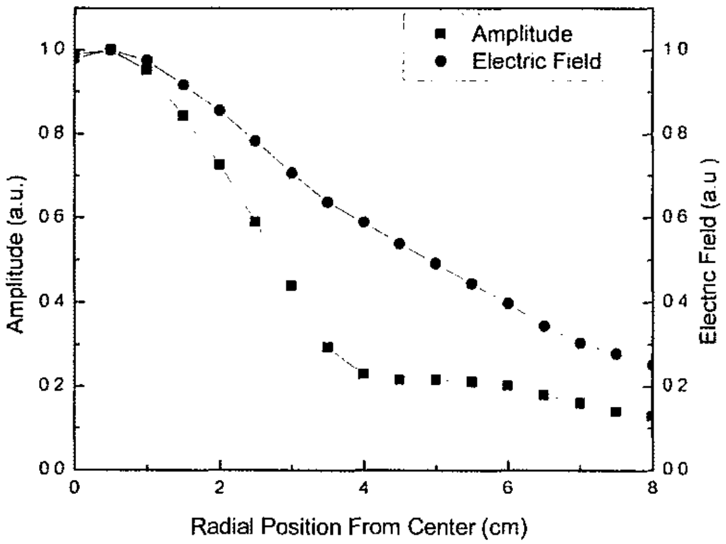

Figure 44: Electric field distribution of the impulse for the shallow focus prolate spheroidal reflector antenna in the radial direction.

Based on the distributions of the UWB impulse-fed shallow focusing antenna and the distribution of the integrated impulse, local maxima and thus focusing is not observed. This result is similar to those for the deep focusing antenna. From the experimental results the electric field distribution in the radial direction shows focusing toward the z-direction axis.

5.4. Electric Field Distribution for Deep Focusing Antenna Fed with Narrowband Signals

The antenna was also evaluated for the use of narrowband signals, centered at 900 MHz and 1500 MHz. The peak-to-peak voltage of the sinusoidal signal was used to determine the electric field distribution. Integration of this measurement is unnecessary because the integration would result in the signal being reversed and the phase altered by 90 degrees, but would not affect the peak-to-peak voltage distribution that is used to evaluate the focusing of the antenna. The results of the electric field distribution evaluation are presented here for both the deep and shallow focusing prolate spheroidal reflector IRA.

In the axial direction, field measurements were made with the probe. Fig. 45 shows the electric field distribution for the narrowband 900 MHz feed signal in the axial direction. Fig. 46 shows the electric field distribution of the 1500 MHz feed signal in the axial direction. From these figures it is evident that there is some focusing. The focusing does occur close to the modeled focal point. However, the distribution at the measured focal point is not as sharp as the model.

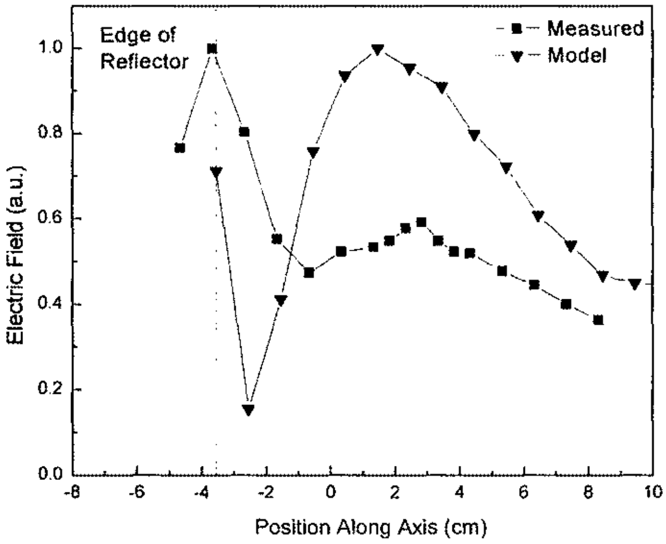

Figure 45: Distribution of the 900 MHz signal for the deep focus prolate spheroidal reflector antenna in the axial direction.

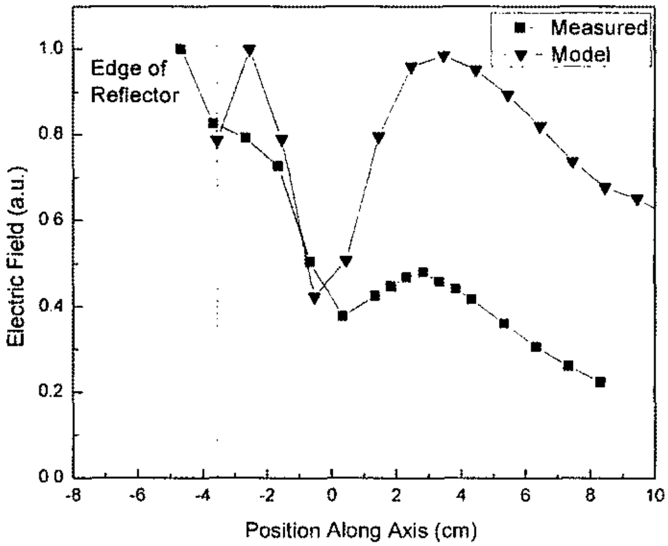

Figure 46: Distribution of the 1500 MHz signal for the deep focus prolate spheroidal reflector antenna in the axial direction.

From the experimental results the antenna appears to be focusing slightly at about 7 centimeters away from the edge of the reflector for the 900 MHz signal and 7.5 centimeters away from the edge for the 1500 MHz signal. Fig. 47 and 48 show the radial distribution, for the two narrowband frequencies at the measured focal points, 7 centimeters away from the edge of the reflector for the 900 MHz signal and 7.5 centimeters from the edge for the 1500 MHz signal. Here the experimental distribution is fairly similar to the modeled radial distribution. However, the measured distribution in the radial direction is wider than the modeled distribution. The faster 1500 MHz signal appears to be closer to the radial modeling distribution than the 900 MHz signal.

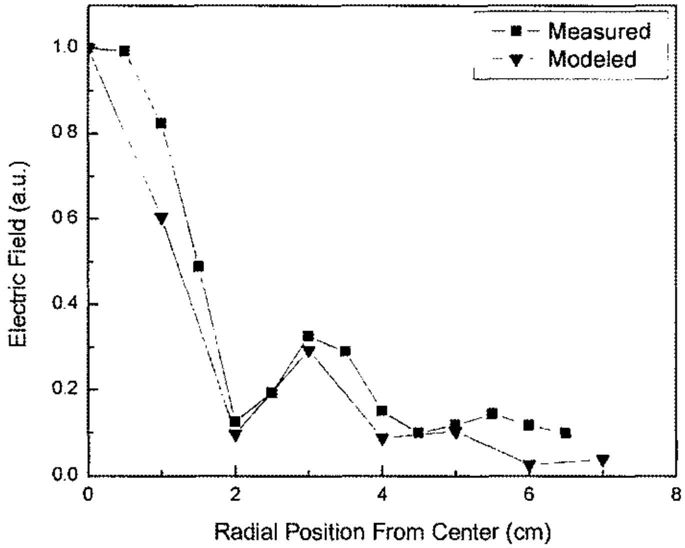

Figure 47: Distribution of the 900 MHz signal for the deep focus prolate spheroidal reflector antenna in the radial direction at the measured focus.

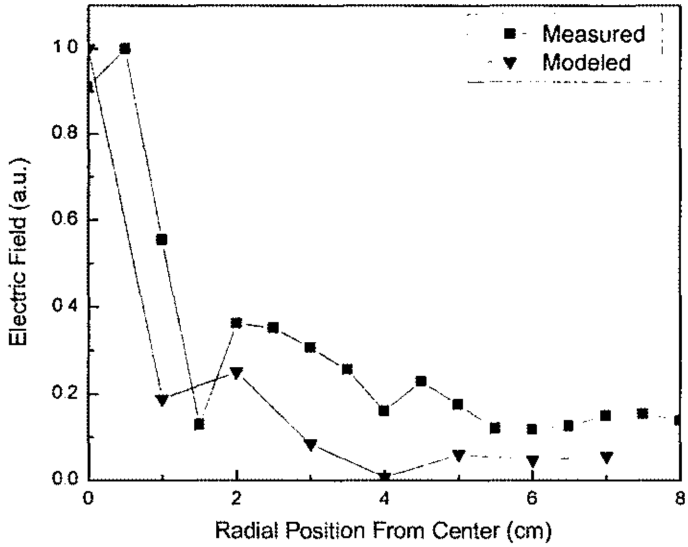

Figure 48: Distribution of the 1500 MHz signal for the deep focus prolate spheroidal reflector antenna in the radial direction at the measured focus.

The size of the focusing spot, or the spot size, can be determined in a variety of ways. In some cases it may be of interest to look at the width of focusing above a certain electric field strength. For this analysis, the spot size will be determined by the full-width, half-maximum values. In the case of this distribution, the full-width, half-maximum values are taken starting from the local minimum located before the observed local maximum. Based on the experimental results the focus spot size for the 900 MHz signal is determined to be 5 centimeters axially by 4 centimeters in the radial direction. The focal spot size of the 1500 MHz signal in the first antenna is about 4 centimeters long in the z-direction and about 3 centimeters long in the radial direction.

5.5. Electric Field Distribution for Shallow Focusing Antenna Fed with Narrowband Signals

Narrowband sinusoidal signals were also evaluated for electric field distribution in the shallow focusing prolate spheroidal reflector IRA. In the axial direction, field measurements were taken. Fig. 49 and 50 display the electric field distribution for the narrowband sinusoidal signals with frequencies of 900 MHz and 1500 MHz, respectively. Here the focal point for the 900 MHz signal appears to be located 3 centimeters away from the edge of the reflector. This matches with the focal point predicted by the model. The shape of the distribution is also very similar to the modeled distribution. The focal point for the 1500 MHz signal appears to be located 3.2 centimeters from the edge. Here the focal point is closer than modeled. However, the shape of the predicted distribution based on the model is very close, though shifted closer to the edge of the reflector for the measured distribution.

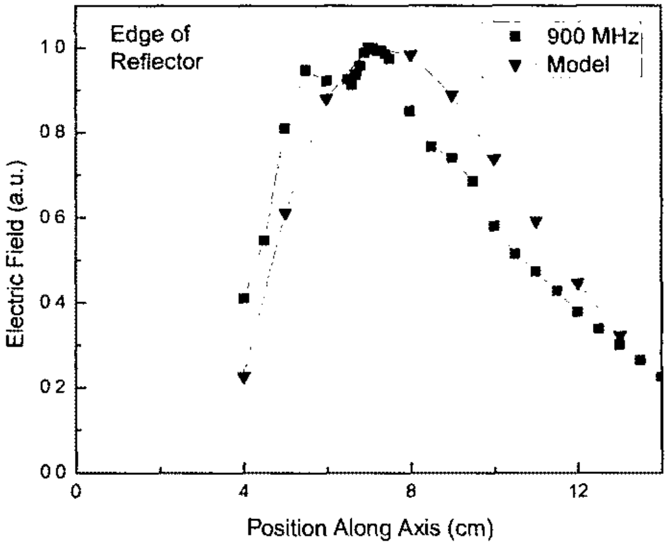

Figure 49: Distribution of the 900 MHz signal for the shallow focus prolate spheroidal reflector antenna in the axial direction.

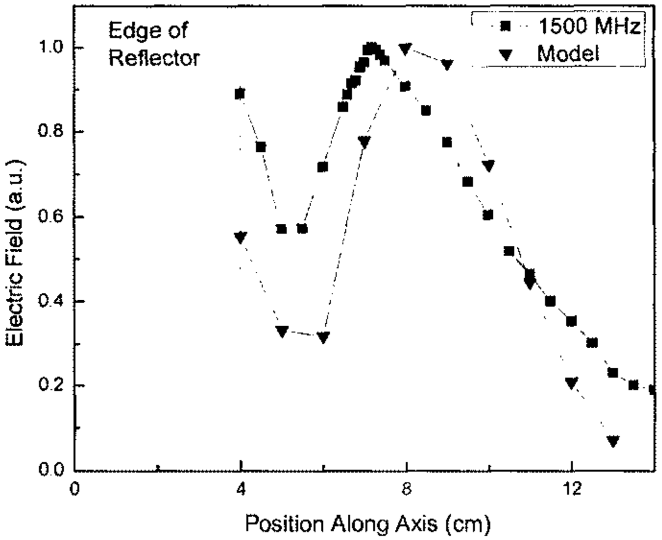

Figure 50: Distribution of the 1500 MHz signal for the shallow focus prolate spheroidal reflector antenna in the axial direction.

Fig. 51 and 52 show the radial distribution at the measured focal point of the previous distributions for the 900 MHz and 1500 MHz feed signals, respectively. The radial distribution also suggests that there is focusing toward the z-direction axis. As with the narrowband feed signal results for the deep focusing antenna, the measured radial distribution appears to be similar to the radial distribution predicted by the model. Both of the distributions are slightly wider than the model predicted. One difference for the distribution of the 1500 MHz feed signal is that about 0.5 centimeters away from the center axis, the electric field seems to increase slightly before it decreases.

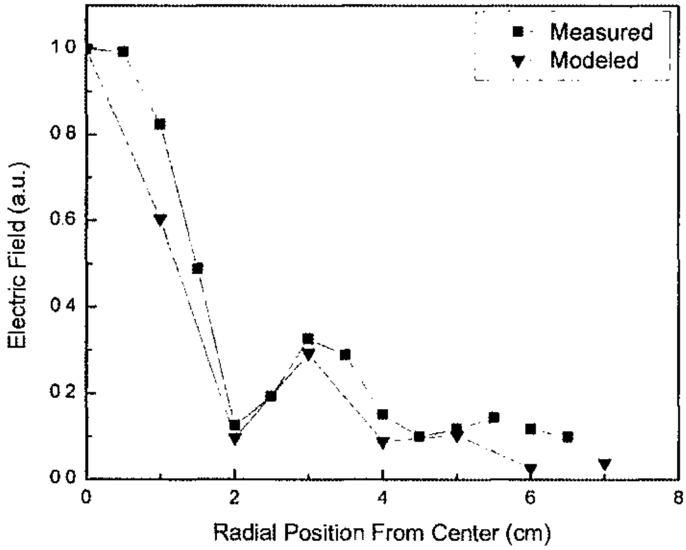

Figure 51: Distribution of the 900 MHz signal for the shallow focus prolate spheroidal reflector antenna in the radial direction at the measured focus.

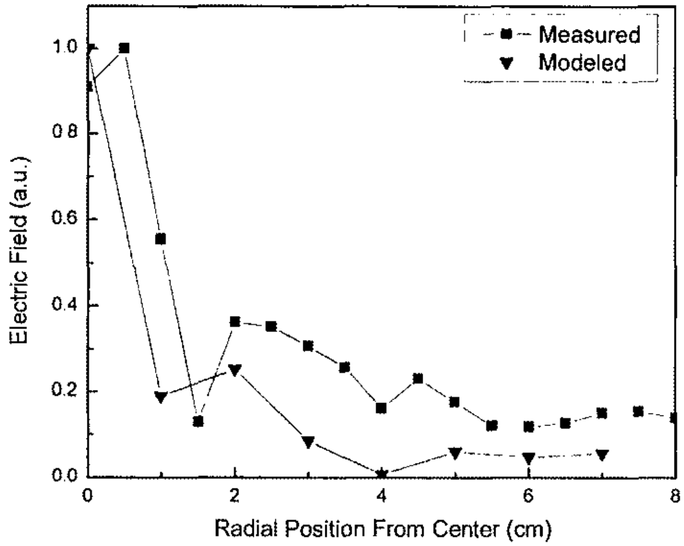

Figure 52: Distribution of the 1500 MHz signal for the shallow focus prolate spheroidal reflector antenna in the radial direction at the measured focus.

Based on the experimental results, the focus spot size for the 900 MHz signal is 3.5 centimeters in the axial direction by 3 centimeters in the radial direction. The focal spot size for the 1500 MHz sinusoidal signal in the shallow focusing antenna is about 4 centimeters long in the z-direction and about 2 centimeters long in the radial direction.

5.6. Summary of Experimental Results

From these results it appears that focusing is not occurring with the UWB-fed signal. However, focusing is occurring when narrowband signals are fed into the antennas. The shallow focusing reflector antenna appears to focus the narrowband signals closer to the model's prediction than the deep focusing reflector antenna.

Table 5 compares the modeled and experimental data for the focusing qualities of each signal type for the supposed long focusing antenna. The table compares the focal point based on geometric analysis, modeled maxima, axial focal length, and radial focal length to the measured quantities. Table 6 compares the modeled and experimental data for the focusing characteristics of each signal type for the shallow focusing depth antenna. The next section will discuss the implications of these results.

Table 5: Comparison of measured and modeled results for the deep focusing prolate spheroidal reflector IRA.

	Pulse	900 MHz	1500 MHz
Geometric Focal Point	(12 cm, 0 cm)	(12 cm, 0 cm)	(12 cm, 0 cm)
Modeled Maxima	(7 cm, 0 cm)	(2 cm, 0 cm)	(4 cm, 0 cm)
Measured Maxima	-------*	(3 cm, 0 cm)	(3 cm, 0 cm)
Modeled Spot Size	4.5 cm x 3 cm	6.5 cm x 3.5 cm	5 cm x 2.5 cm
Measured Spot Size	-------*	5 cm x 4 cm	4 cm x 3 cm

Table 6: Comparison of measured and modeled results for the shallow focusing prolate spheroidal reflector IRA.

	Pulse	900 MHz	1500 MHz
Geometric Focal Point	(9 cm, 0 cm)	(9 cm, 0 cm)	(9 cm, 0 cm)
Modeled Maxima	(9 cm, 0 cm)	(7 cm, 0 cm)	(8 cm, 0 cm)
Measured Maxima	-------*	(7 cm, 0 cm)	(7.2 cm, 0 cm)
Modeled Spot Size	3 cm x 1.5 cm	6 cm x 3 cm	4 cm x 1.5 cm
Measured Spot Size	-------*	3.5 cm x 3 cm	4 cm x 2 cm

*When the antennas were fed with UWB signals, maximum field was observed at the edge of the reflector.

SECTION 6

DISCUSSION

The experimental evaluation of the two reflectors shows that maximum electric field intensity does not occur at the geometric focal point when the antennas are fed with a UWB signal. The first version of the antenna was designed using the deep focusing reflector. In experiments, this antenna, when fed with a UWB signal, did not display a field distribution that agreed with the model. A reflector with a larger a/b ratio was designed with a much shallower focal point. Due to the cosine effect of the focusing radiation as discussed in section 2.2, the axial component of the electric field at the focal point can be increased by providing a larger surface area. Modeling suggested the focus to be much more prominent with this reflector. However, the evaluation of the antenna using this reflector also did not show focusing when fed with a UWB signal. When the reflector was fed with a narrowband signal, the experimental results match well with the model. A local maximum was achieved for the shallow focusing reflector near the geometric focal point, as seen in fig. 49 and 50.

These results suggest that the dispersive properties of water, not accounted for in the modeling software, may have a strong negative effect on focusing. This will be discussed here. These field distributions match very closely to the prediction of the model. A local maximum was observed in the distribution of the antenna with the deep focusing reflector but not close to the geometric focal point, as seen in fig. 45 and 46. The reason the maxima has been shifted from the focus may be the diffraction loss of the deep reflector, which has a smaller reflector area. This diffraction occurs at the reflector edge and will be discussed below.

6.1. Dispersive Properties of Media

For the shallow reflector the ultra-wideband experimental results do not agree with the model. However, the narrowband results do agree with the model. The modeling software does not calculate for the dispersive property of water. For the narrowband-fed signal, dispersion is not an issue. This suggests that the dispersive property of water is the reason the distribution for the antenna with the UWB-fed signal does not agree with the model. Fig. 53 describes the electrical permittivity of water as a function of the frequency of the electromagnetic wave traveling through the water [62]. Equation 6.1.1 describes the complex permittivity of water, including its dependence on the frequency of the wave traveling in the medium.

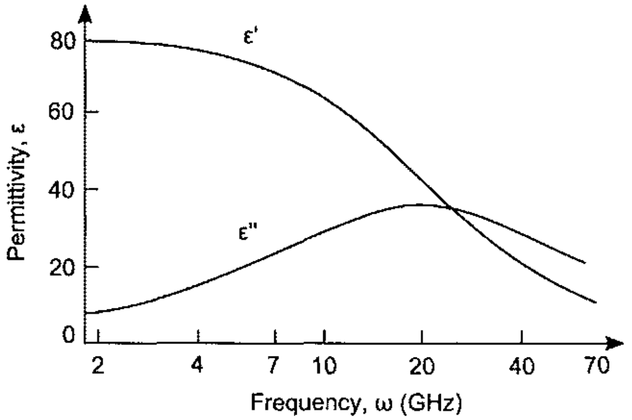

Figure 53: Real and imaginary components of permittivity (ε) of water as functions of frequency (ω) [61].

$$\varepsilon = \varepsilon'(\omega) - j\varepsilon''(\omega) \qquad (6.1.1)$$

The speed of a wave traveling in a medium depends on the electrical properties of the medium, as described in equation 6.1.2. When the medium is water, the wave velocity depends on the permittivity of the water. The ultra-wideband signal that is used encompasses a wide range of frequencies, as shown in fig. 54. Since the permittivity of water depends on the frequency at which the wave is traveling, portions of the ultra-wideband signal will travel at different speeds. The high-frequency components may travel slower than the low-frequency components. As an ultra-wideband signal propagates over a distance, the amplitude of the signal in the time domain decreases and the pulse width broadens. Based on elliptical geometry, the distance the signals traveled from one focal point to the second focal point was 24 centimeters and 18 centimeters for the deep and shallow reflector antennas, respectively. An example of this effect can be seen in fig. 55.

$$v = \frac{c}{\sqrt{\mu_r \varepsilon_r}} \tag{6.1.2}$$

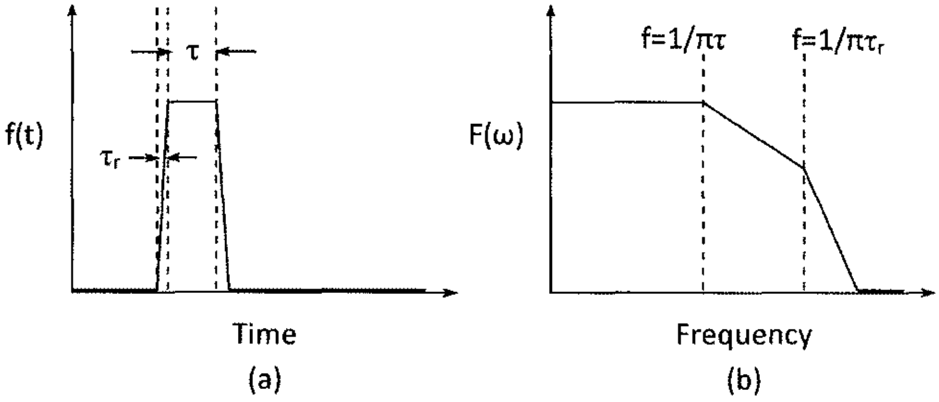

Figure 54: Ultra-wideband pulse in the (a) time domain and (b) frequency domain.

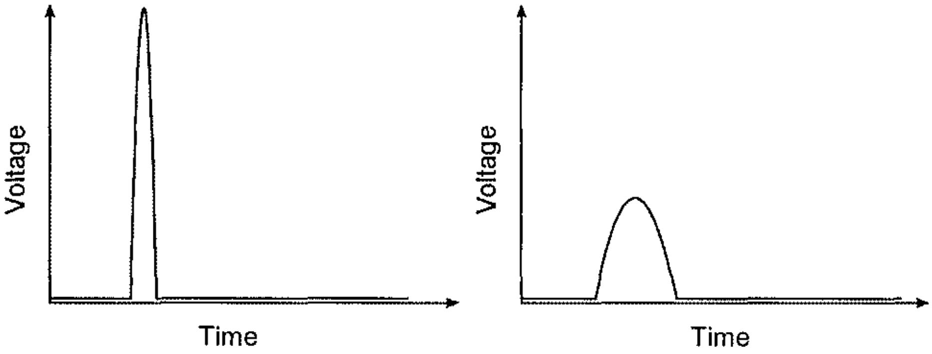

Figure 55: UWB impulse as it travels through a dispersive medium.

The effect of such dispersion on the focusing of these antennas can be shown by comparing of the experimental results for the shallow focusing antenna to the modeled results. Fig. 56 displays the experimental results including the modeling results for an ultra-wideband feed and narrowband feeds. The antennas fed with the UWB signal did not have a maximum electric field at the modeled focal point. However, the antennas fed with the narrowband signals where dispersion is not an issue did exhibit local maxima that agreed with the results from the model. The conductivity of the water medium, which also depends on the frequency of the radiation, may also affect the focusing of the antenna. For the higher frequencies of the radiated signal, the strength of the radiation may be reduced significantly.

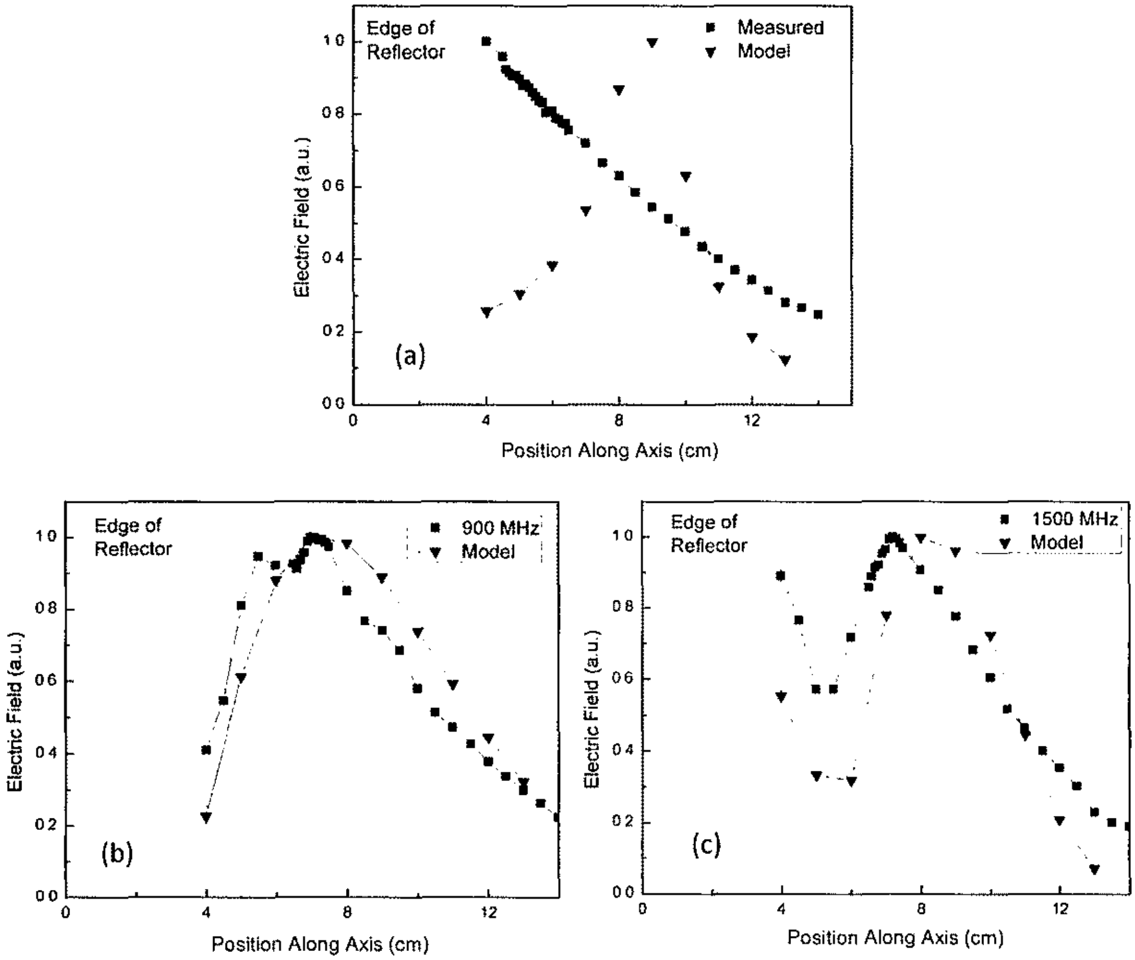

Figure 56: Comparison of the axial distributions for the (a) UWB feed signal and (b) narrowband 900 MHz and (c) 1500 MHz feed signals in the shallow focusing antenna.

6.2. Diffraction at Antenna Structures

Diffraction occurs when an electromagnetic wave passes around an edge. From the modeling it is observed that around the abrupt edges of the conical radiator and reflector, diffraction occurs. The wave is diffracted at these edges, which can act as sources for new spherical waves. The diffracted waves will be considered losses. Some of the signal may be radiated out of the reflector, while some will reflect off the reflector, but because this diffraction wave was introduced away from the focal point, this energy will not contribute to the focusing of the antenna. The effect of the diffraction losses can be shown by the differences between the electric field distributions for the deep and shallow focusing reflectors in the narrow band.

Fig. 57 is a contour plot of the electric fields from the modeling software. This figure shows the diffraction loss at the edge of the reflector. The electric field intensity is higher where the shade is darker. As a result of diffraction some of the energy that is not focused is lost, as is evident in fig. 57, where diffracted radiation can be seen exiting the antenna. The diffraction loss helps to explain why for a deep focusing antenna using the reflector with less surface area when transmitting a narrowband signal displays focusing but closer to the edge of the reflector than the geometric focal point.

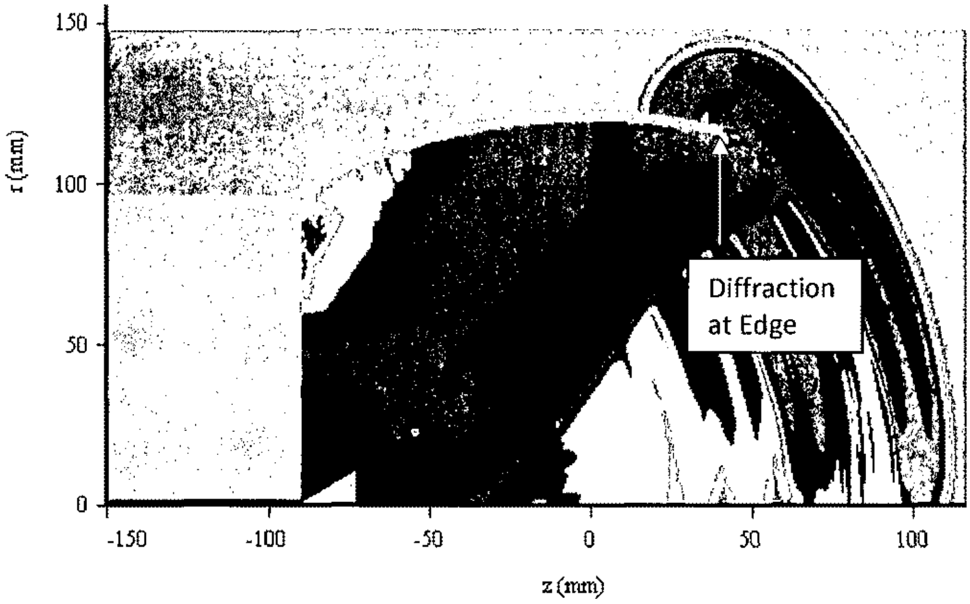

Figure 57: Diffraction occurring at the edge of the reflector.

The reflector area for the shallow focusing antenna is larger than for the deep focusing antenna. The electric field distribution measured for the shallow focusing antenna fed with a narrowband signal shows a maximum located close to the geometric focal point, as shown in fig. 58. For a 900 MHz signal the local maximum is only 2 centimeters closer than the geometric focal point and for a 1500 MHz signal only 1 centimeter closer. In contrast, the electric field distribution measured for the deep focusing antenna fed with a narrowband signal shows a local maximum located 7 centimeters closer than the geometric focal point, as shown in fig. 59. The cosine effect is also a contributing factor when considering the effect of the area of the reflector. As seen in fig. 60, for a large theta, which corresponds to a larger reflector area like the shallow focusing reflector, the cos(θ) component will increase. Similarly as theta is lower, which indicates the smaller reflector like the deep focusing reflector, the cos(θ) component will decrease.

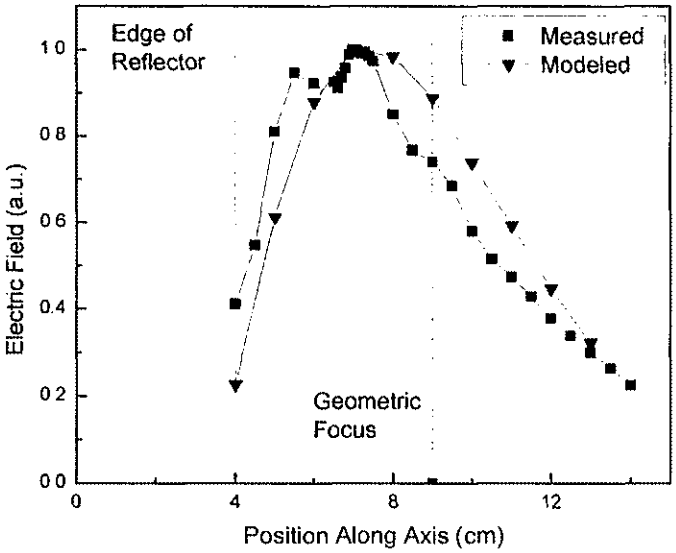

Figure 58: Distribution of the 900 MHz signal for the shallow focus prolate spheroidal reflector antenna in the axial direction.

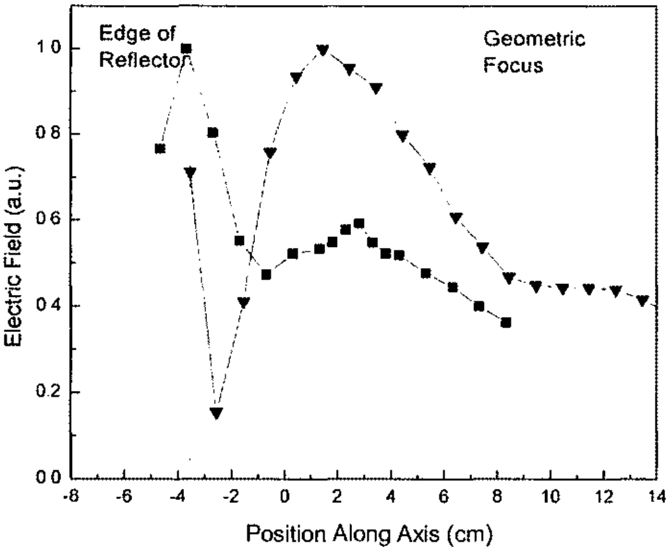

Figure 59: Distribution of the 900 MHz signal for the deep focus prolate spheroidal reflector antenna in the axial direction.

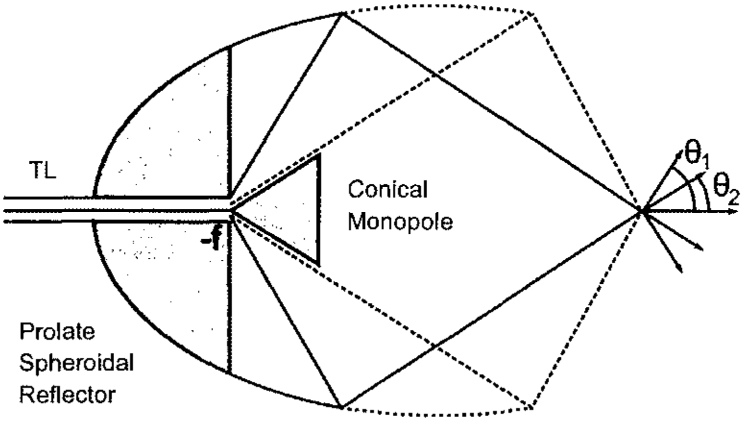

Figure 60: Cosine effect of a shallow (dotted line) and deep (solid line) reflector.

6.3 Improvements to the Antenna

One option to reduce the diffraction is to place a lossy dielectric material at the edges that cause scattering. As shown in fig. 61, a contoured dielectric material, with a high surface-to-volume ratio, could be placed at the end of the conical radiator to absorb much of the signal that is diffracted at the edge, reducing the scattering at the cone edge

[63]. A similar material, possibly a lossy paint, could be placed close to the reflector edge to reduce scattering there as well.

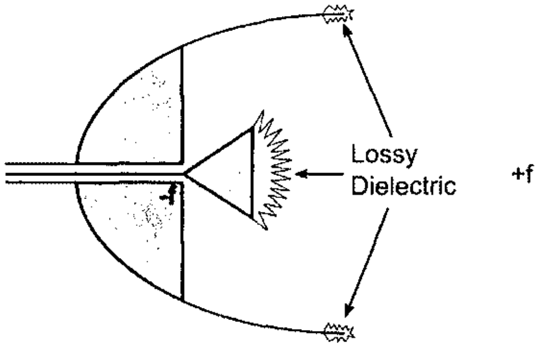

Figure 61: Antenna with lossy dielectric material to reduce diffraction.

Another opportunity to improve the antenna would be to use an asymmetrical structure. For instance, only half of a reflector, halved along the major axis, may be used, as shown in fig. 62. This would allow the focused electric fields to be fully utilized rather than canceling out the field in the radial direction.

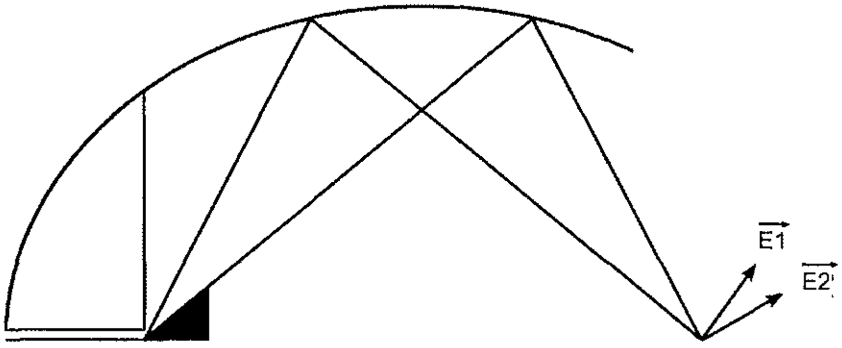

Figure 62: Prolate spheroidal reflector antenna with asymmetrical reflector.

SECTION 7

CONCLUSION

The prolate spheroidal reflector antennas investigated produced a maximum electric field near the edge of the reflectors when fed with ultra-wideband pulses with a rise time of 200 picoseconds, and water as the medium. This can allow high-power, sub-nanosecond pulses to be delivered to a target placed closed to the edge of the reflector for therapeutic and imaging applications.

For narrowband signals the electric field distributions for each of these antennas show focusing occurring up to 7 centimeters away from the edge of the reflector. This would allow one of these reflector antennas to focus narrowband electric fields at a target deeper in the body. This may prove to be a useful application in the field of localized microwave hyperthermia and ablation.

Water as a medium provides a challenge for focusing ultra-wideband signals that must travel a large distance from the first focal point. The attenuation of the water and the dispersive property of water make it difficult to focus ultra-wideband signals outside the reflector. Future modifications such as improvements to the antenna structures may help to achieve focusing for ultra-wideband signals in media.

REFERENCES

[1] S. B. Dev, D.B. Rabussay, G. Widera, G.A. Hofmann, "Medical applications of electroporation," *IEEE Trans. Plasma Science,* vol. 228, pp. 206-223, 2000.

[2] K.H. Schoenbach, S. Xiao, J.T. Camp, "Subnanosecond Electrical Pulses for Medical Therapies and Medical Imaging," in *IEEE International Power Modulators and High Voltage Conference*, 2008, p. 60.

[3] K.H. Schoenbach, S. Xiao, R.P. Joshi, J.T. Camp, T. Heeren, J.F. Kolb, S.J. Beebe, "The Effect of Intense Subnanosecond Electrical Pulses on Biological Cells," *IEEE Trans. Plasma Science,* vol. 36, pp. 414-422, 2008.

[4] K.H. Schoenbach, R. Nuccitelli, S.J. Beebe, "Zap," *Spectrum, IEEE,* vol. 43, pp. 20-26, 2006.

[5] R. Nuccitelli, U. Pliquett, X. Chen, W. Ford, R.J. Swanson, S.J. Beebe, J.F. Kolb, K.H. Schoenbach, "Nanosecond pulsed electric fields cause melanomas to self-destruct," *Biochemical and Biophysical Research Communications,* vol. 343(2), pp. 351-60, 5 May 2006.

[6] K. H. Schoenbach, B. Hargrave, R.P. Joshi, J.F. Kolb, R. Nuccitelli, C. Osgood, A. Pakhomov, M. Stacey, R.J. Swanson, J.A. White, S. Xiao, Z. Jue, S.J. Beebe, P.F. Blackmore, E.S. Buescher, "Bioelectric Effects of Intense Nanosecond Pulses," *IEEE Transactions on Dielectrics and Electrical Insulation,* vol. 14, pp. 1088-1109, 2007.

[7] J. Zhang, P.F. Blackmore, B.Y. Hargrave, S. Xiao, S.J. Beebe, K.H. Schoenbach, "Nanosecond pulse electric field (nanopulse): A novel non-ligand agonist for

platelet activation," *Archives of Biochemistry and Biophysics,* vol. 471, pp. 240-248, 2008.

[8] K. H. Schoenbach, S. Xiao, J.T. Camp, T. Heeren, J.F. Kolb, J.A. White, M. Migliaccio, R.P. Joshi, R. Nuccitelli, S.J. Beebe, C. Baum, S. Altunch, "From Submicrosecond to Subnanosecond Pulses - Entering a New Domain of Electric Field-Cell Interactions," *Plasma Science, IEEE ICOPS,* vol. 2007, p. 474, 17-22 June 2007.

[9] J. T. Camp, S. Xiao, K.H. Schoenbach, "Development of a High Voltage, 150 ps Pulse Generator for Biological Applications," in *Proceedings of the 2008 IEEE International Power Modulators and High Voltage Conference,* pp. 338-341, 2008.

[10] H.P. Schwann, "Electrical properties of tissue and cell suspensions," *Adv. Biol. Med. Phys.,* vol. 5, pp. 147-209, 1957.

[11] M. Lazebnik, D. Popovic, L. McCartney, C.B. Watkins, M.J. Lindstrom, J. Harter, S. Sewall, T. Ogilvie, A. Magliocco, T.M. Breslin, W. Temple, D. Mew, J.H. Booske, M. Okoniewski, S.C. Hagness, "A large-scale study of the ultrawideband microwave dielectric properties of normal, benign and malignant breast tissues obtained from cancer surgeries," *Phys. Med. Biol.,* vol. 52, pp. 6093-6115, 2007.

[12] M. Zhao, J.D. Shea, S.C. Hagness, D.W. van der Weide, B.D. Van Veen, T. Varghese, "Numerical Study of Microwave Scattering in Breast Tissue via Coupled Dielectric and Elastic Contrasts," *IEEE Antennas and Wireless Propagation Letters,* vol. 7, pp. 247-250, 2008.

[13] E. C. Fear, P.M. Meaney, M.A. Stuchly, "Microwaves for breast cancer detection?," *IEEE Potentials,* vol. 22, pp. 12-18, 2003.

[14] S. C. Hagness, A. Taflove, J.E. Bridges, "Two-Dimensional FDTD Analysis of a Pulsed Microwave Confocal System for Breast Cancer Detection: Fixed-Focus and Antenna-Array Sensors," *IEEE Transactions on Biomedical Engineering,* vol. 45, pp. 1470-1479, December 1998.

[15] S.C. Hagness, A. Taflove, J.E. Bridges, "Three-Dimensional FDTD Analysis of a Pulsed Microwave Confocal System for Breast Cancer Detection: Design of an Antenna-Array Element," *IEEE Trans. Ant. Propag.,* vol. 47, pp. 783-791, May 1999.

[16] X. Li, S.C. Hagness, "A Confocal Microwave Imaging Algorithm for Breast Cancer Detection," *IEEE Microwave and Wireless Components Letters,* vol. 11, pp. 130-132, March 2001.

[17] M. Popovic, S.C. Hagness, A. Taflove, "2-D FDTD Study of Fixed-Focus Elliptical Reflector System for Breast Cancer Detection: Frequency Window for Optimum Operation," presented at the IEEE Antennas and Propagation Society International Symposium, 1998.

[18] "First Report and Order," Federal Communications Commission, Washington, DC, 2002.

[19] H. F. Harmuth, *Antennas and Waveguides for Nonsinusoidal Waves.* New York: Academic Press, 1984.

[20] M.G.M. Hussain. Ultra-Wideband Impulse Radar - An Overview of the Principles. *IEEE AES Systems Magazine.* pp. 9-14, 1998.

[21] H. G. Schantz, "A Brief History of UWB Antennas," in *IEEE Conference on Ultra Wideband Systems and Technologies*, 2003.

[22] O. Lodge, "Electric Telegraphy," U.S. Patent, 1898.

[23] P.S. Carter, "Short Wave Antenna," U.S. Patent, 1939.

[24] B. Allen, M. Ghavami, Ed., *Adaptive array systems: fundamentals and applications*. West Sussex, England: John Wiley & Sons Ltd, 2005.

[25] J.R. James, P.S. Hall, C. Wood, Ed., *Microstrip Antenna Theory and Design* (IEE Electromagentic Wave Series 12. London, UK: Peter Peregrinus Ltd, 1986.

[26] V.H. Rumsey, "Frequency Independent Antennas," Presented at the IRE International Convention, 1957.

[27] B. Allen, M. Dohler, E.E. Okon, W.Q. Malik, A.K. Brown, D.J. Edwards, Ed., *Ultra-wideband Antennas and Propagation for Communications, Radar and Imaging*. West Sussex, England: John Wiley & Sons Ltd, 2007.

[28] Y. Mushiake. Self-Complementary Antennas. *IEEE Antennas and Propagation Magazine*. 23-29. Dec. 1992.

[29] N. Behdad, K. Sarabandi, "A multiresonant single-element wideband slot antenna," *IEEE Antennas Wireless Propag. Lett.*, vol. 3, pp. 5–8, 2004.

[30] R. Chair, A.A. Kishk, K.F. Lee, "Ultra-wideband coplanar waveguide-fed rectangular slot antenna," *IEEE Antennas Wireless Propag. Lett.*, vol. 3, pp. 227–229, 2004.

[31] T.G. Ma, S.K. Jeng, "Planar miniature tapered-slot-fed annular slot antennas for ultra-wideband radios," *IEEE Trans. Ant. Propag.*, vol. 53, pp. 1194–1202, Mar. 2005.

[32] G. Sorbello, M. Pavone, L. Rusello, "Numerical and experimental study of a rectangular slot antenna for UWB communications," *Microwave Optical Technol. Lett.,* vol. 46, pp. 315–319, Aug. 2005.

[33] J. Y. Sze, K.L. Wong, "Bandwidth enhancement of a microstripline-fed printed wide-slot antenna," *IEEE Trans. Ant. Propag.,* vol. 49, pp. 1020–1024, Jul. 2001.

[34] I.-J. Yoon, H. Kim, H.K. Yoon, Y.-H. Kim, "Ultra-wideband tapered slot antenna with band cutoff characteristic," *Electron. Lett.,* vol. 41, pp. 629–630, May 2005.

[35] C. E. Baum, A.P. Stone, J.S. Tyo, Ed., *Ultra-Wideband Short-Pulse Electromagnetics 8*. New York, NY: Springer, 2007.

[36] M. Kanda, "The Effects of Resistive Loading of 'TEM' Horns," *IEEE Transactions on Electromagnetic Compatibility,* vol. EMC-24, pp. 245-255, May 1982.

[37] M. Kanda, "A relatively short, cylindrical broadband antenna with tapered resistive loading for picosecond pulse measurement," *IEEE Trans. Ant. Propag.,* vol. AP-26, pp. 439-447, May 1978.

[38] S. Silver, Ed., *Microwave Antenna Theory and Design* (IEE Electromagnetic Waves Series 19. London, UK: Peter Peregrinus Ltd, 1984.

[39] E. G. Farr, "Analysis of the Impulse Radiating Antenna," *Sensor and Simulation Notes*, Note 329, 1991.

[40] C. E. Baum, "Radiation of Impulse-Like Transient Fields," *Sensor and Simulation Notes*, Note 321, 1989.

[41] A. Teggatz, A. Jostingmeier, T. Meyer, A.S. Omar, "Detection of Buried Objects such as Landmines Using a Forward Impulse Radiating Antenna (IRA),"

presented at the IEEE Antennas and Propagation Society International Symposium, 2005.

[42] D.V. Giri, *High-Power Electromagnetic Radiators: Nonlethal Weapons and Other Applications*. Cambridge, MA: Harvard University Press, 2004.

[43] E.G. Farr, C.E. Baum, "Radiation from Self-Reciprocal Apertures," *Sensor and Simulation Notes*, Note 357, 1993.

[44] Y. Manteghi, Y. Rahmat-Samii, "On the Characterization of a Reflector Impulse Radiating Antenna (IRA): Full-Wave Analysis and Measured Results," *IEEE Trans. Ant. Propag.*, vol. 54, pp. 812-822, Mar. 2006.

[45] S. Ghosh, B.K. Sarkar, S.V. Pandey, " Performance characteristics of a reflector Ultra wideband impulse radiating antenna," presented at the 33rd International Conference on Infrared, Millimeter and Terahertz Waves, 2008.

[46] K. Chang, I. Bahl, V. Nair, Ed., *RF and Microwave Circuit and Component Design for Wireless Systems* (Wiley Series in Microwave and Optical Engineering. New York, NY: John Wiley & Sons Ltd, 2002.

[47] C. E. Baum, "Focal waveform of a prolate-spheroidal impulse-radiating antenna," *Radio Sci.*, vol. 42, Nov. 13, 2007.

[48] S. Altunch, C.E. Baum, C.G. Christodoulou, E. Schamiloglu, C.J. Buchenauer, "Focal waveforms for various source waveforms driving a prolate-spheroidal impulse radiating antenna (IRA)," *Radio Sci.*, vol. 43, RS4S13, 2008.

[49] K. Kim, W.R. Scott, "Analysis of Impulse-Radiating Antennas with Ellipsoidal Reflectors," *Sensor and Simulation Notes*, Note 481, 2003.

[50] S. Altunch, C.E. Baum, C.G. Christodoulou, E. Schamiloglu, "Experimental Focal Waveforms of a Prolate Spheroidal Impulse-Radiating Antenna," presented at the EuroEM 08, 2008.

[51] J.H. Jacobi, L.E. Larsen, C.T. Hast, "Water-Immersed Microwave Antennas and Their Application to Microwave Interrogation of Biological Targets," *IEEE Transactions on Microwave Theory and Techniques,* vol. 27, pp. 70-78, Jan. 1979.

[52] I. Yamaura, "Measurements of 1.8-2.7-GHz microwave attenuation in the human torso," *IEEE Transactions on Microwave Theory and Techniques,* vol. 25, pp. 707-710, Aug. 1977.

[53] S. Xiao, M. Migliaccio, J.T. Camp, J.F. Kolb, K.H. Schoenbach, C.E. Baum, "A Wide-Band Focusing System For Bioelectric Applications," presented at the IEEE Pulsed Power and Plasma Science Conference, 2007.

[54] K.H. Schoenbach, S. Xiao, J.T. Camp, M. Migliaccio, S.J. Beebe, C.E. Baum, "Wideband, High-Amplitude, Pulsed Antennas for Medical Therapies and Medical Imaging," Old Dominion University, Norfolk, VA and University of New Mexico, Albuquerque, NM. 2009.

[55] S. Xiao, K.H. Schoenbach, C.E. Baum, "Time-Domain Focusing Radar for Medical Imaging," presented at the XXIX Gen. Assembly of URSI, 2008.

[56] K.S. Yee, "Numerical Solution of Initial Boundary Value Problems Involving Maxwell's Equations in Isotropic Media," *IEEE Trans. Ant. Propag.,* vol. AP-14, pp. 802-807, May 1966.

[57] K.S. Kunz, K. Lee, "A Three-Dimensional Finite-Difference Solution of the External Response of an Aircraft to a Complex Transient EM Environment: Part I - The Method and Its Implementation," *IEEE Transactions on Electromagnetic Compatibility,* vol. EMC20, pp. 328-333, May 1978.

[58] A. Taflove, "Application of the Finite-Difference Time-Domain Method to Sinusoidal Steady-State Electromagnetic-Penetration Problems," *IEEE Transactions on Electromagnetic Compatibility,* vol. EMC22, pp. 191-202, August 1980.

[59] R. Habash, *Bioeffects and Therapeutic Applications of Electromagnetic Energy.* Boca Raton, FL: CRC Press, 2008.

[60] J. Van der Zee, "Heating the patient: a promising approach?," *Ann. Oncol.,* vol. 13, pp. 1173-1184, 2002.

[61] Prodyn, "Electric Field Sensors: Ground Plane." http://www.prodyntech.com/download/ADS10_11.pdf , accessed Sep. 5, 2009.

[62] U. Kaatze, "Complex permittivity of water as a function of frequency and temperature," *J. Chem. Eng. Data,* vol. 34, pp. 371-374, October 1989.

[63] A. Lakhtakia, V.K. Varadan, V.V. Varadan, "Effect of surface texture on absorption by lossy dielectric slabs," *Appl. Opt.,* vol. 25, pp. 4349-4352, 1986.

VITA

Mark A. Migliaccio Jr. was born in Jacksonville, Florida, February 3rd 1986 and resides in Norfolk, Virginia. He received his Bachelor of Science degree in Electrical Engineering with a minor in Computer Engineering from Old Dominion University in Norfolk in the spring of 2008. He has worked as a research assistant at the Frank Reidy Research Center for Bioelectrics at Old Dominion.